Role of strain-rate partitioning in aseismic strain localization: implications for the Karakoram Shear Zone, India

Subham Bose[1], Vikas Adlakha[1], and Shailendra Pundir[2]

[1]Wadia Institute of Himalayan Geology
[2]Wadia Institute of Himalayan Geology, India

November 23, 2022

Abstract

Shear zones in the earth's crust commonly deform by aseismic creep processes which involve localization of strain at varying rates across the shears. Therefore, it is of key importance to quantify the order of strain-rate variation to understand whether deformation was accommodated solely by aseismic or by simultaneous seismic and aseismic slip. The present study demonstrates partitioning of strain-rate between coarse-grained quartz rich layers (CGQL) and amphibole-biotite rich layers (AMBIORL) due to mineralogical and consequently rheological heterogeneities within the mylonitized amphibolites of the Karakoram Shear Zone (KSZ), India. Variations in modal proportion of quartz across the layers resulted in a lower strain rate per unit area accommodated by quartz, in the CGQL than in the AMBIORL that deformed a rate, 2.34-3.43 times higher than the CGQL. Therefore, a considerably higher proportion of dynamically recrystallized quartz nucleated in the AMBIORL. Combined analyses of the proportion of strain-rate partitioning with previously calculated bulk strain-rates suggest that both the CGQL and the AMBIORL deformed by aseismic creep. Thus, strain-rate partitioning due to mineralogical or lithological heterogeneity is a feasible mechanism for strain localization during aseismic creep. Calculated proportion of strain-rate partitioning, when extrapolated to two adjacent lithologically distinct hypothetical layers (at a regional scale), yields differences of 100-200 kilometers, in displacement accommodated by the two layers. Thus, this study suggests that variation in offsets of streams and marker beds, along widely separated segments of the KSZ might well be the manifestations of strain-rate partitioning in the middle-lower crust.

Hosted file

essoar.10507688.1.docx available at https://authorea.com/users/545425/articles/602033-role-of-strain-rate-partitioning-in-aseismic-strain-localization-implications-for-the-karakoram-shear-zone-india

Role of strain-rate partitioning in aseismic strain localization: implications for the Karakoram Shear Zone, India

Subham Bose, Vikas Adlakha*, Shailendra Pundir

Wadia Institute of Himalayan Geology, Dehradun, India

Correspondence to: vikas.himg@gmail.com

Abstract

Shear zones in the earth's crust commonly deform by aseismic creep processes which involve localization of strain at varying rates across the shears. Therefore, it is of key importance to quantify the order of strain-rate variation to understand whether deformation was accommodated solely by aseismic or by simultaneous seismic and aseismic slip. The present study demonstrates partitioning of strain-rate between coarse-grained quartz rich layers (CGQL) and amphibole-biotite rich layers (AMBIORL) due to mineralogical and consequently rheological heterogeneities within the mylonitized amphibolites of the Karakoram Shear Zone (KSZ), India. Variations in modal proportion of quartz across the layers resulted in a lower strain rate per unit area accommodated by quartz, in the CGQL than in the AMBIORL that deformed a rate, 2.34-3.43 times higher than the CGQL. Therefore, a considerably higher proportion of dynamically recrystallized quartz nucleated in the AMBIORL. Combined analyses of the proportion of strain-rate partitioning with previously calculated bulk strain-rates suggest that both the CGQL and the AMBIORL deformed by aseismic creep. Thus, strain-rate partitioning due to mineralogical or lithological heterogeneity is a feasible mechanism for strain localization during aseismic creep. Calculated proportion of strain-rate partitioning, when extrapolated to two adjacent lithologically distinct hypothetical layers (at a regional scale), yields differences of 100-200

kilometres, in displacement accommodated by the two layers. Thus, this study suggests that variation in offsets of streams and marker beds, along widely separated segments of the KSZ might well be the manifestations of strain-rate partitioning in the middle-lower crust.

Plain Language Summary

Variation in strain-rate at the microscopic scale, or strain-rate partitioning across two adjacent mineralogically distinct layers, occurred in the mylonitized amphibolites of the KSZ, due to differences in rheological responses of the layers and the modal proportion of quartz. Strain-rate partitioning resulted in a bimodal grain-size distribution of quartz. Calculated proportion of partitioning of strain-rate between the two mineralogically distinct adjacent layers suggest that both underwent extremely slow slip deformation by aseismic creep. Thus, strain-rate partitioning is a feasible mechanism of strain localization across mineralogically and lithologically distinct zones at diverse scales (micro- to regional) during aseismic creep and can be an important attribute for the considerably variable displacements and hence, offsets along widely separated segments of shears, like the KSZ.

1. Introduction

Strain-rate has always been a parameter of interest in both natural as well as experimental deformation studies, for example, Boutonnet et al. (2013); Fagereng & Biggs (2019); Gleason & Tullis (1995); Hirth et al. (2001); Peternell et al. (2019); Pfiffner & Ramsay (1982); Takahashi et al. (1998). Estimation of strain-rates can be especially significant while investigating active tectonic zones from the combined prespective of the nature and extent of strain accumulation and release (Cannon et al., 2018; Fan and Murphy, 2021; Ojo et al., 2021; Tamura et al., 2020). While strain-rates on the surface are estimated using geodetic techniques (e.g., Gauhlat et al., 2013; Kreemer et al., 2014; Panda et al., 2020) rates of middle to lower crustal deformations are calculated mainly based on deformed quartz, for example strain-rate

formulations of Takahashi (1998) as well as the recent Quartz-strain-rate-metry (QSR) technique devised by Boutonnet et al. (2013). Idea about strain rates becomes increasingly essential when the deformation temperatures are estimated based on the observed microstructures of minerals like feldspar (Ji, 1998; Pryer, 1993; Rosenberg & Stunitz, 2003) and quartz (Hirth & Tullis, 1992; Stipp et al., 2002; Stipp et al., 2010). Although with increasing temperature and decreasing strain rates there is a transition in the recrystallization mechanism of quartz from bulging (BLG) through sub-grain rotation (SGR) to Grain Boundary Migration (GBM) (Law, 2014; Stipp et al., 2002; 2010), not always this transition occurs at conventional strain-rates of Pfiffner & Ramsay, 1982. This is particularly emphasized by Law (2014) by extrapolating the regimes of operation of BLG, SGR and GBM for quartz to the conditions of prevalence of experimental strain-rates. Apart from quantitative estimation of strain-rates (Boutonnet et al., 2013; Pfiffner & Ramsay, 1982; Takahashi et al., 1998) it is also important to characterize high and low strain-rate regimes across natural shear zones. In this context, variation in strain-rates within regional scale ductile shear zones has been documented qualitatively, by Bose and Gupta (2020) based on detailed field and microstructural studies. However, such variation in strain-rates can be present at any scale and thus, the order of variation is especially important to understand whether the variation in strain-rates involved simultaneously operating seismic and aseismic slip. The present study demonstrates a bimodal grain size distribution of quartz in two adjacent mineralogically heterogenous layers due to partitioning of strain-rate at the microscopic scale in the mylonitized amphibolites along the Karakoram Shear Zone (KSZ), India. The proportion of strain-rate partitioning has been utilised to determine whether deformation occurred by seismic and/or aseismic slip in the two adjacent layers. Based on the detailed microstructural observations, heterogenous mineral deformation behaviour along with a difference, between the two layers in terms of the strain-rate accommodated per unit area has been inferred as the key factors for strain-rate

partitioning. Finally, implications of strain-rate partitioning in the middle-lower crust, for variable offsets of streams and marker beds along widely-separated segments of the KSZ have been discussed.

2. Geological setting of the Karakoram Shear Zone

The NW-SE trending dextral KSZ extends from Tash Gurgan in the northwest to Kailash area in the southeast for a distance greater than 1000 km (Boutonnet et al., 2012; Molnar & Tapponnier, 1978; Peltzer & Tapponnier, 1988; Robinson, 2009a; Searle et al., 1998; Tapponnier et al., 1982; Valli et al., 2008; Weinberg et al., 2000; Weinberg et al., 2009; Wallis et al., 2016). The KSZ lies in between the Shyok Suture zone (SSZ), to its southwest and the Tibetan block, to its northeast (Figures 1a and 1b). The SSZ represents junction between cretaceous Ladakh Batholith/arc and Tibetan margin that formed at ~85 Ma (Figure 1a; Borneman et al., 2015; Pundir et al., 2020a). The KSZ is characterized by intensely deformed and mylonitized granite gneisses, slates and sheared phyllites (Pundir et al., 2020a). The right lateral motion along the KSZ is still supposed to be active along some of the segments as reflected by the deflection in the course of the Indus River by 120 Km (Boutonnet et al., 2012; Gaudemer et al., 1989; Robinson et al., 2015). However, there is a lot of debate on the active portions of the fault and especially the rate of displacement along different segments and therefore the offsets. For example, 120 Km (Phillips et al., 2004; Searle et al., 1998), 149-167 km (Robinson, 2009a), greater than 400 Km (Lacassin et al., 2004; Schwab et al., 2004; Valli et al., 2008). Robinson (2009a) speculated that difficulties in estimation of long-term slip rates could be due to dispute over initiation age and tectonic histories of the different segments of the KSZ. This speculation becomes even more important in the light of granulite through amphibolite to greenschist facies metamorphism, reported from different parts of the terrane (Rolland et al., 2009).

Thus, apart from determining activity along specific segments of the KSZ in the present-day it is also important to characterize the ductile deformation underwent along the different segments of this zone during late Oligocene to mid-Miocene and more importantly the processes that operated during the deformation. Given this background, the present study documents micro-scale strain-rate partitioning in the mylonitized amphibolites across the Tangtse-Muglib mylonitic strands of the KSZ (Figure 1b; Borneman et al., 2015; Boutonnet et al., 2012; Boutonnet et al., 2013; Pundir et al., 2020a; 2020b; Searle et al., 1998; Searle and Philips, 2007; Sen et al., 2014; Wallis et al., 2016; Weinberg et al., 2000). It has been demonstrated that partitioning of strain-rate occurred between mineralogically distinct adjacent layers and the variable offsets along different segments of the KSZ can be manifestations of similar processes operating at various scales (micro- to- regional) in the present-day middle to lower crust.

3. Methodology

Major lithologies as well as the planar and linear structural fabrics in the Karakoram terrane were mapped mainly across the Tangtse-Muglib and the Darbuk-Shyok transects (Figure 1b), respectively. Oriented samples were collected from suitable outcrops and the planar and the linear structural data were plotted on Equal area projection diagrams. Oriented thin sections from the less-deformed as well as the mylonitized strands of the Karakoram Shear Zone (KSZ) were prepared from the oriented samples. The oriented thin sections were studied under a petrographic microscope and the major minerals were identified. Detailed microstructures of the major minerals were studied along with nature of deformation (rigid or plastic) of the different minerals along the KSZ. Recrystallization mechanism of quartz and feldspar were identified on the basis of microstructural criteria in accordance with Kruhl and Nega (1996), Stipp et al. (2002), Vernon (2004), Passchier and Trouw (2005) and Stipp et al. (2010). Based on these recrystallization mechanisms, the deformation temperatures were

estimated at previously estimated strain-rates of the order of 10^{-13} by Boutonnet et al. (2013) for the KSZ. Qualitative identification of high strain-rate micro-domains have been carried out on the basis of the proportion of nucleated recrystallized grains, the higher the proportion of recrystallized grains the higher is the strain-rate and vice-versa (Jia et al. 2009; Peternell et al., 2019). Moreover, Bose & Gupta (2020) correlated consistent increase in the proportion of dynamically recrystallized grains with an apparent reduction in competency contrast between feldspar and quartz which in turn was inferred as an outcome of increasing strain-rate by Vigneresse (2004). The positive correlation between strain rate and the proportion of dynamically recrystallized grains is also implied by the Orowan equation (Hull & Bacon, 1986; Karato, 2008) which suggests that

$$\dot{\epsilon} = b\boldsymbol{\rho v}, \qquad (1)$$

where, $\dot{\epsilon}$ is the strain-rate, b is the burgers vector, ρ is the dislocation density and v is the dislocation velocity. This implies that in the absence of considerable strain-hardening (ρ does not vary significantly with strain rate) extent of dislocation creep increases with strain rate; a greater extent of dislocation creep is manifested in a higher proportion of dynamically recrystallized grains (Tullis et al., 2000; Vernon, 2004). Thus, in the absence of considerable strain-hardening, zones with a higher proportion of dynamically recrystallized grains can be correlated with higher strain rates (Jia et al., 2019), while lower strain rate zones are characterized by a higher proportion of relict (non-recrystallized) clasts. The ratio of the strain-rates between two micro-domains has been calculated using a combination of the ductile rheological law (Gleason & Tullis, 1995) and the different piezometers of Twiss (1977), Stipp & Tullis (2003) and Shimizu (2008). The strain accommodated by a particular micro-domain has been calculated by multiplying the strain-rate with the duration of deformation and has been converted into displacement using the equation of Fagereng and Biggs, 2019:

$$\gamma = d/w \qquad (2)$$

where, γ is the shear strain, d is the displacement parallel to the boundaries of the zone that had undergone shear deformation at a particular rate and w is the width of the zone that had been deformed during shearing.

Based on the above methods, micro-scale partitioning of strain-rate has been demonstrated between two adjacent micro-domains which can be used to explain aseismic strain localization in outcrop as well as in regional scale.

4. Results

4.1. Lithology and structure

Major lithounits exposed along the Tangtse-Muglib strand include mylonitised amphibolites and granite gneisses (Figure 2a). The mylonitic foliation strikes NW-SE (Figures 1b & 2b) and dips steeply either towards NE or SW (Figure 1b). Granite gneisses, in contact with the amphibolites preserve a prominent segregation between the feldspathic and the quartz-rich layers (Figure 2b). The feldspathic layers, generally pinch out within the apparently less competent quartz-rich layers (Figure 2b) and exhibit a prominent dextral asymmetry in plan (Figure 2b). On the surface of the mylonitic foliation (S; Figures 2c & d) a subhorizontal stretching lineation (L) is detected (Figures 2c & d) which is conformable with the observed dextral asymmetry (Figure 1b) in plan.

4.2. Microstructure

4.2.1. Granite gneisses

The mylonitic foliation in the granite gneisses (location TM 1 in Figure 1b) is defined by an alternate segregation between feldspathic and quartz-rich layers as also observed on ground (Figure 2b). Both these layers are essentially monomineralic in nature (Figure 3a) with sharp distinct boundaries between the two and is devoid of any cusps and lobes or interfingering along the boundaries (Figure 3a). Within the quartz-rich layers interfingering is observed along amoeboid grain boundaries (Figure 3b) that exhibit sutures with wavelengths of the order of the grain size (Kruhl & Nega, 1998; Vernon, 2004) implying pre-dominant GBM recrystallization (Stipp et al., 2002; Vernon, 2004). Lack of any layered arrangement of uniform-sized recrystallized grains precludes the possibility of significant recrystallisation by subgrain rotation (SGR; Stipp et al., 2002), at least in the studied lithounits. This implies that deformation temperature was above ~550 ℃ (Stipp et al., 2002) if conventional strain rates (Pfiffner & Ramsay, 1982; Law, 2014) are assumed. On the other hand, in the feldspathic domains core-mantle structures (Figure 3c) are observed with a mantle of recrystallized grains surrounding relict feldspar cores (Figure 3c). Sharp, distinct boundaries between the core and the recrystallized mantle (Figure 3c) suggest that the feldspars underwent recrystallization by bulging (BLG) mechanism that occurs at temperatures, not more than ~600 ℃. Thus, microstructural studies carried out on the mylonitic fabric-defining minerals i.e., feldspar and quartz reveal prevailing temperatures in between ~550-600 ℃ during the dextral shearing event. Importantly, Boutonnet et al. (2013) calculated strain rates of the order of $10^{-13}\ \ s^{-1}$ by applying quartz-strain-rate-metry (QSR) on the lithounits deformed along the mylonitic strands of the KSZ.

4.2.2. Mylonitized amphibolites

In the relatively low strain zones (locations DS6-DS8 in Fig. 1b), the foliation is defined by a preferred orientation of biotite (Figures 3d & 3e) and quartz ribbons (Figure 3e). Within the quartz ribbons, grain boundaries of quartz exhibit amoeboid sutures (Figure 3e) with

196 wavelengths of the order of the grain-size. This implies that quartz grains recrystallized by
197 grain boundary migration (GBM), similar to that in the granite gneisses. Importantly, the
198 amphiboles do not show any considerable preferred orientation (Figures 3d-3f) in these low
199 strain zones, unlike the biotites, and appear to have deformed by fracturing and rotation of
200 mechanical fragments. Deformed lamellar twins or wedge twins are observed in plagioclase
201 feldspar.

202 The mylonitized amphibolites (location TM 2 in Fig. 1b; Figures 2a & 2d), in contact
203 with the granite gneisses along the mylonitic strands of the KSZ, preserve the mylonitic
204 foliation (concordant with that in the gneisses) along with a subhorizontal stretching lineation
205 on the foliation (Figure 2d). Therefore, in all probability, the amphibolites were also
206 subjected to dextral shearing along with the granite gneisses at ~550-600 °C. Within the
207 mylonitized amphibolites, quartz grains exhibit an approximate bimodal grain-size
208 distribution (Figures 4a-4d) with coarser-grained monomineralic quartz-rich layers (CGQL;
209 Figures 4a-4f) and finer-grained quartz-amphibole-biotite rich layers (AMBIORL; Figures
210 4a-4d & 4f). Coarser quartz grains in the monomineralic layers with very few amphiboles and
211 biotite grains (Figures 4b & d-f) have amoeboid boundaries with interfingering contacts
212 (Figures 4e & 4f). Sutures along the boundaries have wavelengths of the order of the grain
213 size, implying GBM as the recrystallization mechanism in quartz, similar to that in the lower
214 strain zones and the granite gneisses (Figure 3b). However, a significant reduction in grain
215 size of quartz is observed in the fine-grained layers (Figures 4a-4d & 4f), which also contain
216 a considerable proportion of amphibole and biotite (Figures 4a-d & 4f). This significant
217 reduction in grain size implies a higher rate of nucleation of quartz in the fine-grained layers,
218 which might result from a greater extent of dynamic recrystallization of quartz. This
219 proposition becomes even more evident as ribbons of quartz, sandwiched between
220 amphiboles and biotites, are also detected in the fine-grained layers (Figures 4b & 4f). As the

temperature of deformation did not exceed ~600 ℃, pinning of quartz by amphibole and biotite in the fine-grained layers is manifested in the form of quartz grains with straight grain boundaries at high angles to the foliation, occurring within the ribbons (Figures 4b, 4d & 4f). Nevertheless, the grain sizes in the finer-grained layers appear to be the characteristic of bulging recrystallization mechanism (BLG; Stipp et al., 2002; 2010), although no preserved evidence of BLG mechanism (bulges with wavelengths of an order significantly lower than that of the grain-size) have been detected (Figures 3 & 4). Moreover, in the coarser-grained layers, quartz-grains indicate recrystallization by GBM. These layers do not apparently preserve deformation bands and sub-grain boundaries, which generally indicate a higher internal strain within the individual grains. This is in disagreement with BLG mechanism that is much more likely to be associated with micro-domains in which quartz grains preserve a higher internal strain, at least under conventional strain rates (Pfiffner & Ramsay, 1982), similar to the prevalent conditions (strain rate ~ 10^{-13} s^{-1}; Boutonnet et al., 2013) in the present case. Even within the fine-grained layers, there is variation in grain- size with relatively finer grains adjacent to microdomains with a higher modal proportion of amphibole and biotite and vice versa (Figures 4c, 4d & 4f). Thus, the extent of nucleation of quartz grains appears to be related somehow to the proportion of amphiboles and biotites.

5. Discussion

Mylonitized amphibolites and granite gneisses, exposed along the Tangtse-Muglib strands of the dextral KSZ, underwent deformation at ~550-600 ℃ under conventional strain rates. The amphiboles and the biotites in the amphibolites had a tendency to segregate into layers alternating with coarser-grained, monomineralic quartz-rich domains with increasing strain during dextral shearing. Within the amphibole-biotite-rich layers (AMBIORL) in the mylonitized amphibolites, the quartz grains are significantly finer than those in the monomineralic coarse-grained quartz-rich layers (CGQL). This can be either due to the

recrystallization of quartz by BLG (Stipp et al., 2002; 2010) in the AMBIORL and/or considerably greater grain nucleation during dynamic recrystallization than that in the CGQL. Other than the grain size of quartz, the AMBIORL and the CGQL also differ in the modal proportion of amphiboles and biotites. Therefore, it becomes important to investigate the mechanism of fining of quartz grains in the AMBIORL to determine whether the fining is related to the higher modal proportion of amphiboles and biotites.

5.1. Finer quartz in the AMBIORL: BLG or higher grain-nucleation rate?

The gross grain size of quartz in the fine-grained layers (AMBIORL) is similar to the size of those grains, which reportedly forms during BLG recrystallization of quartz (Figures 4b & d; Stipp et al., 2002; 2010). However, the absence of any crosscutting relationship between the AMBIORL and the CGQL (Figure 4), along with the parallelism of these two layers (Figure 4), suggests that both these layers deformed simultaneously. Apart from this, the granite gneisses in contact with the mylonitized amphibolites do not preserve any evidence of BLG recrystallization, although the mesoscopic mylonitic foliation in the two lithologies is in concordance with each other. Microstructural features of feldspar and quartz in both the lithologies undoubtedly indicate deformation temperatures to ~550-600 °C. Therefore, it is very much unlikely that even if BLG operated in quartz in the AMBIORL, locally in microscopic scale, it was not associated with deformation temperatures of ~280-400 °C (Stipp et al., 2002) at which BLG in quartz generally operates under conventional strain rates (Figure 5; Stipp et al., 2002; 2010). Moreover, the prevalence of ~280-400 °C temperatures is difficult to visualize exclusively in the AMBIORL, which does not show any crosscutting relationship with the mesoscopic foliation and the CGQL and especially when GBM, in general, is the pre-dominant recrystallization mechanism in quartz. Thus, BLG, if occurred at all, must have operated under strain rates of 10^{-8} to 10^{-9} s^{-1} (Figure 5), which is at least about 10^{4} to 10^{5} times higher than the conventional strain rates (Pfiffner &

Ramsay, 1982) at 550-600 ℃ (Fig. 5). On the contrary, theoretical estimates using Fig. 5 suggest that GBM in the coarse-grained layers could not have operated at strain rates higher than about $10^{-11}\ s^{-1}$ at 550-600 ℃ (Figure 5). Based on QSR, Boutonnet et al. (2013) inferred strain rates greater than 1.6 x $10^{-13}\ s^{-1}$ along the mylonitic strands of the KSZ. Therefore, based on a combination of the strain rate data of Boutonnet et al. (2013) and undoubted evidence of GBM recrystallization in quartz, the strain-rate in the CGQL can be constrained in the range of 1.6 x 10^{-13} to $10^{-11}\ s^{-1}$ at 550-600 ℃ (Figure 5; Boutonnet et al., 2013). Thus, if BLG and GBM in quartz operated simultaneously in the AMBIORL and the CGQL, respectively, then quartz in the AMBIORL must have deformed at a rate of about 10^2 to 10^5 times higher than the quartz in the CGQL (Figure 5). In this context, the higher nucleation of quartz grains in the AMBIORL can be attributed to a higher rate of dynamic recrystallization in the AMBIORL than in the CGQL. Nucleation of grains during deformation is often positively correlated with strain rate (Peternell et al., 2019; Jia et al., 2009), i.e., a higher strain-rate will lead to an increase in the nucleation of grains, as also inferred quantitatively by the experimental studies of Peternell et al. (2009). Bose and Gupta (2020) systematically correlated a higher proportion of recrystallized feldspar and quartz with a consistent apparent reduction in competency-contrast between these two minerals, which in turn indicates a higher strain-rate by the global model of Vigneresse (2004). Therefore, in the absence of significant strain hardening in the quartz grains, the proportion of nucleated dynamically recrystallized grains is likely to increase with an increase in strain rate. Thus, a difference exists in the rate of deformation of quartz between the CGQL and the AMBIORL. In other words, irrespective of the operation of BLG and/or higher grain nucleation rate (than the CGQL) in the AMBIORL, strain-rate partitioning occurred between the CGQL and the AMBIORL on the microscopic scale. However, it is yet to be determined, whether the

295 proportion of strain-rate partitioning was sufficient to cause simultaneous operation of GBM
296 and BLG in the quartz grains in the CGQL and the AMBIORL, respectively.

297 **5.2. Proportion of partitioning of strain-rate between CGQL and AMBIORL**

298 Although strain-rate partitioning in between the CGQL and the AMBIORL becomes
299 evident from the discussions above, the proportion in which the partitioning occurred is yet to
300 be understood. Determination of the proportion of strain-rate partitioning can have
301 implications for simultaneous seismic and/or aseismic slip partitioning in mico-scale. We
302 assessed the proportion of partitioning of strain-rate between the CGQL and the AMBIORL
303 using a combination of the ductile rheological law (Gleason & Tullis, 1995) and the
304 piezometric equations (Shimizu, 2008; Stipp & Tullis, 2003; Twiss, 1977). The ductile
305 rheological law has been used in accordance with the formulation of Gleason and Tullis
306 (1995) as follows:

307 $$\dot{\varepsilon} = d\varepsilon/dt = A.\sigma^{n}.e^{-QRT} \quad (3)$$

308 Where Q is the activation energy, A is a material parameter, R is the ideal gas constant, T is
309 the temperature, σ is the flow stress, and n, the stress exponent = 4 (derived experimentally).

310 Piezometric equations applied in calculation include:

311 $\sigma = K_{(Twiss,1977)}.D^{-0.68}$; after Twiss (1977);

312 where, $K_{(Twiss,1977)}$ is the constant in the piezometric equation of Twiss (1977)

313 $\sigma = K_{(Stipp\ and\ Tullis,\ 2003)}.D^{-0.794}$; after Stipp and Tullis (2003)

314 where, $K_{(Stipp\ and\ Tullis,\ 2003)}$ is the constant in the piezometric equation of Stipp and Tullis
315 (2003)

316 $\sigma = K_{(Shimizu,\ 2008)}.D^{-0.8}$; after Shimizu (2003)

where, $K_{(Shimizu,\ 2008)}$ is the constant in the piezometric equation of Shimizu (2008)

The mean grain size (D; Table 1) has been calculated based on optical studies and as per the formulations of Christie and Ord (1980).

For the CGQL, combination of ductile rheological law and piezometric equations yields

$\dot{\varepsilon} = \mathrm{A}.K_{(Twiss,1977)}.(4.64\ x\ 10^{-3}).e^{-QRT}$; σ substituted after Twiss (1977) (7)

$\dot{\varepsilon} = \mathrm{A}.K_{(Stipp\ and\ Tullis,\ 2003)}.(1.87\ x\ 10^{-3})e^{-QRT}$; σ substituted after Stipp and Tullis (2003)

(8)

$\dot{\varepsilon} = \mathrm{A}.K_{(Shimizu,\ 2008)}.(1.66\ x\ 10^{-3})e^{-QRT}$; σ substituted after Shimizu (2008) (9)

For the AMBIORL, combination of ductile rheological law and piezometric equations yields

$\dot{\varepsilon} = \mathrm{A}.K_{(Twiss,1977)}.(1.085\ x\ 10^{-2})e^{-QRT}$; σ substituted after Twiss (1977) (10)

$\dot{\varepsilon} = \mathrm{A}.K_{(Stipp\ and\ Tullis,\ 2003)}.(6.27\ x\ 10^{-3})e^{-QRT}$; σ substituted after Stipp and Tullis (2003)

(11)

$\dot{\varepsilon} = \mathrm{A}.K_{(Shimizu,\ 2008)}.(5.69\ x\ 10^{-3})e^{-QRT}$; σ substituted after Shimizu (2008) (12)

Based on these equations (7-12), it has been estimated that quartz in the AMBIORL deformed at a rate 2.34-3.43 times higher than that in the CGQL as per the following calculations:

$\dot{\varepsilon}_{AMBIORL}/\dot{\varepsilon}_{CGQL} = (1.085\ x\ 10^{-2})/(4.64\ x\ 10^{-3})$; dividing equation (10) by equation (7)

337 = 2.34 (13)

338

339 $\dot{\varepsilon}_{AMBIORL}/\dot{\varepsilon}_{CGQL}$ = $(6.27\ x\ 10^{-3})/\ (1.87\ x\ 10^{-3})$; dividing equation (11) by equation (8)

340 = 3.35 (14)

341 $\dot{\varepsilon}_{AMBIORL}/\dot{\varepsilon}_{CGQL}$ = $(5.69\ x\ 10^{-3})/\ (1.66\ x\ 10^{-3})$; dividing equation (12) by equation (9)

342 = 3.43 (15)

343 Therefore, the partitioning of strain-rate in the AMBIORL is about $10^0 - 10^1$ times
344 higher than that in the CGQL. Thus, it can be inferred that the finer grain-size of quartz in the
345 AMBIORL was solely due to micro-scale strain-rate partitioning and not due to any BLG
346 recrystallization mechanism that, on the other hand, would require the quartz in the
347 AMBIORL to deform at a rate 10^2 to 10^5 times higher than the quartz in the CGQL, as
348 discussed in section 4.1. Moreover, as the AMBIORL deformed at a rate, 2.34-3.43 times
349 higher than the CGQL then displacement accomdated in 12 Ma (duration of shearing along
350 the KSZ as per Pundir et al., 2020b) by the AMBIORL and the CGQL is 0.92 cm and 2.79-
351 4.1 cm (see Appendix), respectively. This displacement values imply extremely slow slip as
352 categorized by Nielsen (2017). Therefore, neither of the two layers deformed at high strain
353 rates and were involved in any seismic slip that is generally associated with velocities in the
354 order of ms^{-1} (Nielsen, 2017) and strain-rates of $1\ to 10^2\ s^{-1}$ (Kreemer et al., 2014;
355 Fagereng and Biggs, 2019). Thus, partitioning of strain-rate at the microscopic scale between
356 the CGQL and the AMBIORL, was associated with extremely slow slip deformation by
357 aseismic creep in both the layers. In accordance with observations and calculations, slow
358 aseismic creep was more localized in the AMBIORL than in the CGQL. So, strain-rate

359 partitioning can be a very common mechanism for strain localization during aseismic creep
360 across any scale especially in the presence of mineralogical and lithological heterogeneities.

361 **5.3. Partitioning of strain-rate: why and how?**

362 At temperatures of 550-600 ℃, although feldspar and quartz can undergo deformation
363 by dislocation creep, amphibole is more likely to deform by fracturing and mechanical
364 rotation due to its reported brittle-ductile transition at least above 700 ℃ (Passchier & Trouw,
365 2005). For example, Ross and Wilks (1996) inferred simultaneous plastic deformation of
366 plagioclase by dislocation creep and fracturing and mechanical rotation of fragments of
367 hornblende. Nevertheless, the preferred orientation of amphiboles in the high strain zones
368 (Figures 4b-4d), unlike in the relatively lower strain zones (Figures 3d; Figure 6a), suggests
369 that the amphiboles underwent rigid rotation towards the finite extension direction in the high
370 strain zones (Figures 6b-6c). Fracturing in amphiboles could have also occurred under
371 conditions when the applied stress exceeded the yield strength of amphiboles. On the other
372 hand, Biotites deformed plastically with ease at ~550-600 ℃ as the brittle-ductile transition
373 for biotite occurs at temperatures as low as 150-250 ℃ (Passchier & Trouw, 2005). However,
374 biotite can deform only by slip on the basal plane along the <100> and the <110> directions
375 (Passchier & Trow, 2005). In this context, it is noteworthy that biotite belongs to the
376 monoclinic crystal system, with very few symmetry elements. As a result, plastic deformation
377 of biotite can occur by slip on only one suitably oriented slip plane along very few slip
378 directions, unlike quartz, which, due to the presence of a larger number of symmetry
379 elements (trigonal or hexagonal crystal system), can accommodate deformation by slip along
380 any of the six <a> directions on several crystallographic planes (Abalos et al., 2016; Hobbs,
381 1985; Mainprice et al., 1986; Schmid and Casey, 1986; Twiss and Moores, 1992). Thus,
382 although biotite in the AMBIORL underwent plastic deformation during shearing along the
383 KSZ, the availability of very few slip systems may well have restricted the biotites from

384 accommodating the bulk of the strain. Under this situation, the bulk of the strain in the
385 AMBIORL was undoubtedly partitioned into the quartz-bearing domains (adjacent to
386 amphiboles and biotites), especially at temperatures where quartz can deform easily by slip
387 along any of the a-axes on several crystallographic planes.

388 Summarising the above facts, in the low strain zones of the KSZ, the foliation in the
389 amphibolites is defined mainly by a preferred orientation of biotites, and amphiboles do not
390 show any significant alignment (Figure 6a). The amphiboles and biotites were segregated into
391 distinct micro-domains with increasing strain (AMBIORL in Figure 6b). The bulk of the
392 strain on the AMBIORL was localized into the quartz-bearing domains (Figure 6b) as
393 amphiboles did not undergo ductile deformation, and the biotites accommodated limited
394 strain. The occurrence of amphiboles and biotites in the AMBIORL, resulted in (a) the
395 localization of strain in the quartz-rich domains of the AMBIORL with strain on the quartz
396 grains naturally decreasing with distance from the amphiboles and biotites and (b) effective
397 reduction of the areal proportion of quartz in any particular area (e.g., A in Figure 6b) in the
398 AMBIORL than that in a similar area (A) in the CGQL (Figure 6b).

399 Thus, strain accommodated per unit area over any time interval (t) by quartz in the
400 AMBIORL will be higher than the strain per unit area on the quartz over the same time
401 interval (t) in the CGQL. As a result, the rate of deformation of quartz in the AMBIORL
402 must have been higher than that in the CGQL. A higher deformation rate in the AMBIORL
403 resulted in higher nucleation of dynamically recrystallized grains in the AMBIORL than in
404 the CGQL (Figure 6c).
405

406 **5.4. Implications of strain-rate partitioning for the KSZ**

Micro-scale partitioning of strain-rate as discussed above for the mylonitized amphibolites along the Tangtse-Muglib strand of the KSZ is promoted by an increase in mineralogical and, therefore, rheological heterogeneity as demonstrated in section 5.3. Considering that the KSZ deformed continuously from ~27-15 Ma (Pundir et al., 2020b), at a bulk strain rate of 1.6 x 10^{-13} s^{-1} (Boutonnet et al., 2013), a bulk strain of 60.5 and 141.6-207.5 (see Appendix) were accommodated by the CGQL and the AMBIORL, respectively, in the mylonitized amphibolites. For orthogonal thicknesses of w = 152.3 µm and w' = 197.1 µm (Figure 4d; Fig. 7a), for example, for the CGQL and the AMBIORL, respectively, displacement accommodated by the CGQL will be 0.92 cm (Fig. 7a; see Appendix), whereas in the AMBIORL will accommodate a displacement of 2.79-4.1 cm (Figure 7a, see Appendix), as per equation (2). Therefore, even in the scale of a thin section, displacement accommodated by the AMBIORL will be 1.87-3.18 cm greater than that accommodated by the CGQL ((see Appendix; Figure 7a). If a similar proportion of strain-rate partitioning and hence the accommodated strain are extrapolated to two adjacent deformed hypothetical layers, each 10 meters thick (outcrop scale; Figure 7b), then displacement in layer 2 that accommodated higher bulk strain will be about 800-1500 meters greater than that in the less deformed layer 1 (Figure 7b, see Appendix). If similar extrapolation is done on two adjacent hypothetical layers, each 1.25 km thick (Figure 7c; regional scale; total thickness 2.5 km similar to the width of the Tangtse strand in Figure 1b), then layer 2 (more deformed) will accommodate a displacement of about 100-200 km greater than that accommodated by the less-deformed layer 1 (Figure 7c, see Appendix). It is noteworthy that the calculations for Figures 7b and 7c are based on hypothetical layers between which strain-rate has been assumed to have partitioned in a proportion similar to that between the AMBIORL and the CGQL. Therefore, the calculated displacement should not supposedly represent the actual displacement along the Tangtse strand of the KSZ (Figure 1b). Nevertheless, variations in

offsets, similar to that calculated in Figure 7c, are observed along widely separated segments of the KSZ (Robinson, 2009a). Therefore, the calculations using hypothetical layers in Figures 7b & 7c has just been carried out to assess an estimate of the order of difference in displacements accommodated by any two mineralogically and/or lithologically and hence rheologically distinct layers between which strain-rate has been partitioned at a given proportion. Thus, considering the natural lithological and hence rheological heterogeneity across the shear zone on a regional scale, significant differences in accommodated displacement between two adjacent layers are bound to occur even along any single segment of the approximately 1000 km long KSZ. This implies that the displacements along widely dispersed segments of the KSZ are likely to vary significantly, which is actually the case (Robinson, 2009b). Presently and also in the Quarternary, ductile deformation at mid-crustal depths of the lithospheric scale KSZ (Paul et al., 2021) must have involved similar strain-rate partitioning across diverse scales which might very well be responsible for the observed differences in offsets of marker beds and streams across the widely separated segments of the shear (Lacassin et al., 2004; Phillips et al., 2004; Robinson, 2009a; Schwab et al., 2004; Searle et al., 1998; Valli et al., 2008).

6. Conclusion

During ductile deformation, rigid minerals incapable of ductile flow and minerals that undergo limited plastic deformation can lead to micro-scale partitioning of the rate of deformation of the mineral that can easily undergo plastic deformation. Partitioning of strain-rate along natural shear zones is promoted by increasing mineralogical, lithological, and therefore rheological heterogeneities, which leads to the accommodation of strain at a higher

rate in the heterogeneous layers. Therefore, a higher strain accommodation occurs over a particular lateral distance across any shear zone.

Partitioning of strain-rate in between the CGQL and the AMBIORL in the mylonitized amphibolites along the KSZ involved slow aseismic creep and was not associated with any fast-slip seismic events. Thus, strain-rate partitioning appears as an important mechanism of strain localization during aseismic creep.

In the context of the KSZ, strain-rate partitioning between mineralogically heterogenous layers of the same lithology and between different lithologies can account for variable displacement even across any single segment of the shear. Thus, KSZ, being a 1000 km long lithospheric shear zone, must have transected different lithologies and hence different rheologies in the vertical and horizontal directions due to which variability in displacement along different segments of the shear appears to be a natural phenomenon. Similar processes must have occurred at middle to lower crustal depths, along and across the lithospheric KSZ, from Quarternary to the present. The manifestations of the variation in displacements in the ductile regime can very well be the variable offsets of marker beds and streams across the Karakoram Fault, now observed on the surface.

Acknowledgements

Data used in this study is available in Mendeley Data, Version 1, doi: 10.17632/rzjphcs8v7.1, (**https://data.mendeley.com/datasets/rzjphcs8v7/1**). This work was supported by Science and Engineering Research Board grant EMR/2014/000555 and Wadia Institute of Himalayan Geology grant Activity 7c of CAP-Himalaya awarded to Vikas Adlakha. Manoranjan Mohanty and Rajwant of Department of Science and Technology (DST) and Science and Engineering Research Board (SERB), New Delhi, respectively, are thanked for their continuous support and encouragement. Discussions with Koushik Sen improved the paper.

Chhutapa Phuntsog Dorjay, Skalzang Namgyal, and Thinless Gyachho are thanked for field assistance. The Indo-Tibetan Border Police (ITBP) is highly acknowledged for help during fieldwork in the Ladakh, NW India. We also thank Saibal Gupta of IIT Kharagpur, Ramesh Chandra Patel of BHU Varanasi and Director, WIHG for encouragement.

References

Ábalos, B., Puelles, P., Fernández-Armas, S., & Sarrionandia, F. (2011). EBSD microfabric study of pre-Cambrian deformations recorded in quartz pebbles from the Sierra de la Demanda (N Spain). *Journal of Structural Geology*, *33*(4), 500-518. https://doi.org/10.1016/j.jsg.2011.01.005

Borneman, N.L., Hodges, K.V., Van Soest, M.C., Bohon, W., Wartho, J.A., Cronk, S.S., Ahmad, T. (2015). Age and structure of the Shyok suture in the Ladakh region of northwestern India: Implications for slip on the Karakoram fault system. *Tectonics*, *34*(10), 2011-2033. https://doi.org/10.1002/2015TC003933

Bose, S., & Gupta, S. (2020). Evolution of stretching lineations in granulite-hosted ductile shear zones, Eastern Ghats Province, India: Role of temperature, strain rate and pre-existing stretching lineations. *Journal of Structural Geology*, *138*, 104127. https://doi.org/10.1016/j.jsg.2020.104127

Boutonnet, E., Leloup, P.H., Arnaud, N., Paquette, J.L., Davis, W.J., & Hattori, K. (2012). Synkinematic magmatism, heterogeneous deformation, and progressive strain localization in a strike-slip shear zone: The case of the right-lateral Karakorum fault. *Tectonics*, *31*(4). https://doi.org/10.1029/2011TC003049

Boutonnet, E., Leloup, P.H., Sassier, C., Gardien, V., & Ricard, Y. (2013). Ductile strain rate measurements document long-term strain localization in the continental crust. *Geology*, *41*(8), 819-822. https://doi.org/10.1130/G33723.1

Cannon, J.M., Murphy, M.A., & Taylor, M. (2018). Segmented strain accumulation in the High Himalaya expressed in river channel steepness. *Geosphere*, *14*(3), 1131–1149. https://doi.org/10.1130/GES01508.1

Christie, J.M., & Ord, A. (1980). Flow stress from microstructures of mylonites: example and current assessment. *Journal of Geophysical Research: Solid Earth*, *85*(B11), 6253-6262. https://doi.org/10.1029/JB085iB11p06253

Fagereng, Å., & Biggs, J. (2019). New perspectives on 'geological strain rates' calculated from both naturally deformed and actively deforming rocks. *Journal of Structural Geology*, *125*, 100-110. https://doi.org/10.1016/j.jsg.2018.10.004

Fan, S., & Murphy, M.A. (2021).Three-dimensional strain accumulation and partitioning in an arcuate orogenic wedge: An example from the Himalaya. *Geological Society of America Bulletin*, *133*(1-2), 3-18. https://doi.org/10.1130/B35528.1

Gahalaut, V.K., Kundu, B., Laishram, S.S., Catherine, J., Kumar, A., Singh, M.D., Tiwari, R.P., Chadha, R.K., Samanta, S.K., Ambikapathy, A., & Mahesh, P. (2013). Aseismic plate boundary in the Indo-Burmese wedge, northwest Sunda Arc. *Geology*, 41(2), 235-238. https://doi.org/10.1130/G33771.1

Gaudemer, Y., Tapponnier, P., & Turcotte, D.L. (1989). River offsets across active strike-slip faults.

Gleason, G.C., & Tullis, J. (1995). A flow law for dislocation creep of quartz aggregates determined with the molten salt cell. *Tectonophysics*, *247*(1-4), 1-23. https://doi.org/10.1016/0040-1951(95)00011-B

525 Hirth, G., & Tullis, J.A.N. (1992). Dislocation creep regimes in quartz aggregates. *Journal of*
526 *Structural Geology*, *14*(2), 145-159. https://doi.org/10.1016/0191-8141(92)90053-Y
527 Hobbs, B.E. (1985). The hydrolytic weakening effect in quartz. *Point Defects in Minerals*,
528 *31*, 151-170. https://doi.org/10.1029/GM031p0151
529 Hull, D., & Bacon, D.J. (2001). *Introduction to dislocations*. Butterworth-Heinemann.
530
531 Ji, S. (1998). Deformation Microstructure of Natural Plagioclase. In Fault-related Rocks (pp.
532 276-277). Princeton University Press. https://doi.org/10.1515/9781400864935.276
533 Jia, Z., Gao, Z., Ji, J., Liu, D., Guo, T., & Ding, Y. (2019). Study of the dynamic
534 recrystallization process of the Inconel625 alloy at a high strain rate. *Materials*,
535 *12*(3), 510. https://doi.org/10.3390/ma12030510
536 Karato, S. (2008). *Deformation of Earth Materials*. Cambridge University Press, Cambridge.
537 Kreemer, C., Blewitt, G., & Klein, E.C. (2014). A geodetic plate motion and Global Strain
538 Rate Model. *Geochemistry, Geophysics, Geosystems*, *15*(10), 3849-3889.
539 https://doi.org/10.1002/2014GC005407
540 Kruhl, J.H., & Nega, M. (1996). The fractal shape of sutured quartz grain boundaries:
541 application as a geothermometer. *Geologische Rundschau*, *85*(1), 38-43.
542 Lacassin, R., Valli, F., Arnaud, N., Leloup, P.H., Paquette, J.L., Haibing, L., Tapponnier, P.,
543 Chevalier, M.L., Guillot, S., Maheo, G., Zhiqin, X. (2004). Large-scale geometry,
544 offset and kinematic evolution of the Karakorum fault, Tibet. *Earth and Planetary*
545 *Science Letters*, *219*(3-4), 255-269. https://doi.org/10.1016/S0012-821X(04)00006-8
546 Law, R.D. (2014). Deformation thermometry based on quartz c-axis fabrics and
547 recrystallization microstructures: A review. *Journal of Structural Geology*, *66*, 129-
548 161. https://doi.org/10.1016/j.jsg.2014.05.023

549 Mainprice, D., Bouchez, J.L., Blumenfeld, P., & Tubià, J.M. (1986). Dominant c slip in
550 naturally deformed quartz: Implications for dramatic plastic softening at high
551 temperature. *Geology*, *14*(10), 819-822. https://doi.org/10.1130/0091-
552 7613(1986)14<819:DCSIND>2.0.CO;2
553 Molnar, P., & Tapponnier, P. (1978). Active tectonics of Tibet. *Journal of Geophysical*
554 *Research: Solid Earth*, *83*(B11), 5361-5375.https://doi.org/10.1029/JB083iB11p05361
555 Nielsen, S. (2017). From slow to fast faulting: recent challenges in earthquake fault
556 mechanics. Philosophical Transactions Royal Society A 375: 20160016.
557 http://dx.doi.org/10.1098/rsta.2016.0016
558 Ojo, A.O., Kao, H., Jiang, Y., Craymer, M., & Henton, J. (2021). Strain Accumulation and
559 Release Rate in Canada: Implications for Long-Term Crustal Deformation and
560 Earthquake Hazards. *Journal of Geophysical Research Solid Earth.*
561 https://doi.org/10.1029/2020JB020529
562 Panda, D., Kundu, B., Gahalaut, V.K., & Rangin, C. (2020). India-Sunda plate motion,
563 crustal deformation, and seismic hazard in the Indo-Burmese Arc. Tectonics, 39(8),
564 p.e2019TC006034. https://doi.org/10.1029/2019TC006034
565 Passchier, C.W., & Trouw, R.A. (2005). *Microtectonics*. Springer Science & Business Media.
566 Paul, A., Hazarika, D., Wadhawan, M., & Kumar, N. (2021). Upper mantle anisotropy in the
567 northwest Himalaya and Ladakh-Karakoram zone based on SKS splitting analysis.
568 *Journal of Geodynamics*, *144*, 101817. https://doi.org/10.1016/j.jog.2021.101817
569 Peltzer, G., & Tapponnier, P. (1988). Formation and evolution of strike-slip faults, rifts, and
570 basins during the India-Asia collision: An experimental approach. *Journal of*
571 *Geophysical Research: Solid Earth*, *93*(B12), 15085-15117.
572 https://doi.org/10.1029/JB093iB12p15085

573 Peternell, M., Wilson, C.J., & Hammes, D.M. (2019). Strain rate dependence for evolution
574 of steady state grain sizes: Insights from high-strain experiments on ice. *Earth and*
575 *Planetary Science Letters*, *506*, 168-174. https://doi.org/10.1016/j.epsl.2018.10.037
576 Pfiffner, O.A., & Ramsay, J.G. (1982). Constraints on geological strain rates: arguments from
577 finite strain states of naturally deformed rocks. *Journal of Geophysical Research:*
578 *Solid Earth*, *87*(B1), 311-321. https://doi.org/10.1029/JB087iB01p00311
579 Phillips, R.J., Parrish, R.R., & Searle, M.P. (2004). Age constraints on ductile deformation
580 and long-term slip rates along the Karakoram fault zone, Ladakh. *Earth and*
581 *Planetary Science Letters*, *226*(3-4), 305-319.
582 https://doi.org/10.1016/j.epsl.2004.07.037
583 Pryer, L.L. (1993). Microstructures in feldspars from a major crustal thrust zone: the
584 Grenville Front, Ontario, Canada. *Journal of structural Geology*, *15*(1), 21-36.
585 https://doi.org/10.1016/0191-8141(93)90076-M
586 Pundir, S., Adlakha, V., Kumar, S., & Singhal, S. (2020a). Closure of India–Asia collision
587 margin along the Shyok Suture Zone in the eastern Karakoram: new geochemical and
588 zircon U–Pb geochronological observations. *Geological Magazine*, *157*(9), 1451-
589 1472. https://doi.org/10.1017/S0016756819001547
590 Pundir, S., Adlakha, V., Kumar, S., Singhal, S., & Sen, K. (2020b). Petrology, geochemistry
591 and geochronology of granites and granite gneisses in the SE Karakoram, India:
592 Record of subduction-related and pre-to syn-kinematic magmatism in the Karakoram
593 Fault Zone. *Mineralogy and Petrology*, *114*(5), 413-434.
594 https://doi.org/10.1007/s00710-020-00706-y
595 Robinson, A.C. (2009a). Geologic offsets across the northern Karakorum fault: Implications
596 for its role and terrane correlations in the western Himalayan-Tibetan orogen. *Earth*

597 *and Planetary Science Letters*, *279*(1-2), 123-130.
598 https://doi.org/10.1016/j.epsl.2008.12.039
599 Robinson, A.C. (2009b). Evidence against Quaternary slip on the northern Karakorum Fault
600 suggests kinematic reorganization at the western end of the Himalayan–Tibetan
601 orogen. *Earth and Planetary Science Letters*, *286*(1-2), 158-170.
602 https://doi.org/10.1016/j.epsl.2009.06.025
603 Robinson, A.C., Owen, L.A., Chen, J., Schoenbohm, L.M., Hedrick, K.A., Blisniuk, K.,
604 Sharp, W.D., Imrecke, D.B., Li, W., Yuan, Z., & Caffee, M.W. (2015). No late
605 Quaternary strike-slip motion along the northern Karakoram fault. *Earth and*
606 *Planetary Science Letters*, *409*, 290-298. https://doi.org/10.1016/j.epsl.2014.11.011
607 Rolland, Y., Mahéo, G., Pecher, A., & Villa, I.M. (2009). Syn-kinematic emplacement of the
608 Pangong metamorphic and magmatic complex along the Karakorum Fault (N
609 Ladakh). *Journal of Asian Earth Sciences*, *34*(1), 10-25.
610 https://doi.org/10.1016/j.jseaes.2008.03.009
611 Rosenberg, C.L., & Stünitz, H. (2003). Deformation and recrystallization of plagioclase along
612 a temperature gradient: an example from the Bergell tonalite. *Journal of Structural*
613 *Geology*, *25*(3), 389-408. https://doi.org/10.1016/S0191-8141(02)00036-6
614 Ross, J.V., & Wilks, K.R. (1996). Microstructure development in an experimentally sheared
615 orthopyroxene granulite. *Tectonophysics*, *256*(1-4), 83-100.
616 https://doi.org/10.1016/0040-1951(95)00168-9
617 Schmid, S.M., & Casey, M. (1986). Complete fabric analysis of some commonly observed
618 quartz c-axis patterns. *Geophysical Monograph*, *36*(6), 263-286.
619 Schwab, M., Ratschbacher, L., Siebel, W., McWilliams, M., Minaev, V., Lutkov, V., Chen,
620 F., Stanek, K., Nelson, B., Frisch, W., & Wooden, J.L. (2004). Assembly of the
621 Pamirs: Age and origin of magmatic belts from the southern Tien Shan to the

southern Pamirs and their relation to Tibet. *Tectonics*, *23*(4). https://doi.org/10.1029/2003TC001583

Searle, M.P., & Phillips, R.J. (2007). Relationships between right-lateral shear along the Karakoram fault and metamorphism, magmatism, exhumation and uplift: evidence from the K2–Gasherbrum–Pangong ranges, north Pakistan and Ladakh. *Journal of the Geological Society*, *164*(2), 439-450. https://doi.org/10.1144/0016-76492006-072

Searle, M.P., Weinberg, R.F., & Dunlap, W.J. (1998). Transpressional tectonics along the Karakoram fault zone, northern Ladakh: constraints on Tibetan extrusion. *Geological Society, London, Special Publications*, *135*(1), 307-326. https://doi.org/10.1144/GSL.SP.1998.135.01.20

Sen, K., Mukherjee, B.K., & Collins, A.S. (2014). Interplay of deformation and magmatism in the Pangong Transpression Zone, eastern Ladakh, India: Implications for remobilization of the trans-Himalayan magmatic arc and initiation of the Karakoram Fault. *Journal of Structural Geology*, 62, 13-24. https://doi.org/10.1016/j.jsg.2014.01.009

Shimizu, I. (2008). Theories and applicability of grain size piezometers: The role of dynamic recrystallization mechanisms. *Journal of Structural Geology*, *30*(7), 899-917. https://doi.org/10.1016/j.jsg.2008.03.004

Stipp, M., & Tullis, J. (2003). The recrystallized grain size piezometer for quartz. *Geophysical Research Letters*, *30*(21). https://doi.org/10.1029/2003GL018444

Stipp, M., Stünitz, H., Heilbronner, R., & Schmid, S.M. (2002). Dynamic recrystallization of quartz: correlation between natural and experimental conditions. *Geological Society, London, Special Publications*, *200*(1), 171-190. https://doi.org/10.1144/GSL.SP.2001.200.01.11

646 Stipp, M., Tullis, J., Scherwath, M., & Behrmann, J.H. (2010). A new perspective on
647 paleopiezometry: Dynamically recrystallized grain size distributions indicate
648 mechanism changes. *Geology*, *38*(8), 759-762. https://doi.org/10.1130/G31162.1
649 Takahashi, M., Nagahama, H., Masuda, T., & Fujimura, A. (1998). Fractal analysis of
650 experimentally, dynamically recrystallized quartz grains and its possible application
651 as a strain rate meter. *Journal of structural Geology*, *20*(2-3), 269-275.
652 https://doi.org/10.1016/S0191-8141(97)00072-2
653 Tamura, T., Oohashi, K., Otsubo, M., Miyakawa, A., & Niwa, M. (2020). Contribution to
654 crustal strain accumulation of minor faults: a case study across the Niigata–Kobe
655 Tectonic Zone, Japan. *Earth, Planets and Space*, *72* (7).
656 https://doi.org/10.1186/s40623-020-1132-5
657 Tapponnier, P., Peltzer, G.L.D.A.Y., Le Dain, A.Y., Armijo, R., & Cobbold, P. (1982).
658 Propagating extrusion tectonics in Asia: New insights from simple experiments with
659 plasticine. *Geology*, *10*(12), 611-616.
660 https://doi.org/10.1130/0091-7613(1982)10<611:PETIAN>2.0.CO;2
661
662 Tullis, J., Stünitz, H., Teyssier, C., & Heilbronner, R. (2000). Deformation microstructures in
663 quartzo-feldspathic rocks. *Journal of the Virtual Explorer*, *2*.
664 10.3809/jvirtex.2000.00019
665 Twiss, R.J. (1977). Theory and applicability of a recrystallized grain size paleopiezometer. In
666 *Stress in the Earth* (227-244). Birkhäuser, Basel. 10.1007/978-3-0348-5745-1_13
667 Twiss, R.J., & Moores, E.M. (1992). *Structural geology*. Macmillan.
668 Valli, F., Leloup, P.H., Paquette, J.L., Arnaud, N., Li, H., Tapponnier, P., Lacassin, R.,
669 Guillot, S., Liu, D., Deloule, E., & Xu, Z. (2008). New U-Th/Pb constraints on

timing of shearing and long-term slip-rate on the Karakorum fault. *Tectonics*, *27*(5). https://doi.org/10.1029/2007TC002184

Vernon, R.H. (2004). *A practical guide to rock microstructure*. Cambridge university press.

Vigneresse, J.L., & Burg, J.P. (2004). Strain-rate-dependent rheology of partially molten rocks. *Geological Society, London, Special Publications*, *227*(1), 327-336. https://doi.org/10.1144/GSL.SP.2004.227.01.17

Wallis, D., Carter, A., Phillips, R.J., Parsons, A.J., & Searle, M.P. (2016). Spatial variation in exhumation rates across Ladakh and the Karakoram: New apatite fission track data from the Eastern Karakoram, NW India. *Tectonics*, *35*(3), 704-721. https://doi.org/10.1002/2015TC003943

Weinberg, R.F., Dunlap, W.J., & Whitehouse, M. (2000). New field, structural and geochronological data from the Shyok and Nubra valleys, northern Ladakh: linking Kohistan to Tibet. *Geological Society, London, Special Publications*, *170*(1), 253-275. https://doi.org/10.1144/GSL.SP.2000.170.01.14

Weinberg, R.F., Mark, G., & Reichardt, H. (2009). Magma ponding in the Karakoram shear zone, Ladakh, NW India. *Geological Society of America Bulletin*, *121*(1-2), 278-285. https://doi.org/10.1130/B26358.1

Figure captions

Figure 1 a) Map of the Karakoram terrane. Study area is represented by the red-coloured dashed box. Inset shows the Karakoram terrane on the map of India (adapted and modified after Pundir et al., 2020b). b) Geological map of the area showing the major lithologies, the planar and linear structural elements (adapted and modified after Pundir et al., 2020b). The Tangtse and the Muglib strands of the Karakoram Shear Zone (KSZ) are marked in orange colour. The present work is based primarily on locations TM 1 and TM 2 along the Tangtse

695 strand of the KSZ and the locations DS 6, DS 7 and DS 8 in the relatively less deformed part
696 of the Tangtse Metamorphic Complex (TMC). Sample TM 2 is the key focus of this study.

697 **Figure 2** Field photographs a) Granite gneiss and mylonitized amphibolite occurring in
698 contact along the Tangtse strand of the KSZ. Note the concordance of the planar fabric (S) in
699 the two lithologies. b) Dextrally sheared feldspathic domains in plan in the granite-gneisses
700 along the KSZ. c) Sub-horizontal stretching lineation (L) on the steeply dipping mylonitic
701 foliation surface in the granite gneisses along the KSZ. d) Sub-horizontal stretching lineation
702 on the steeply dipping mylonitic foliation (S) in the mylonitized amphibolites.

703 **Figure 3** Photomicrographs: a) Foliation in the granite gneisses, defined by alternate
704 monomineralic layers of feldspar and quartz. Note the segregation between the feldspathic
705 and the quartz-rich layers. b) Amoeboid sutures along the boundaries of quartz with the
706 quartz ribbons. Note the deformation bands within some of the quartz grains. c) Core-mantle
707 structure in feldspar. Note the sharp boundary between the core and the mantle of
708 recrystallized grains. d) amphibole, biotite, feldspar and quartz in the deformed amphibolites
709 of the Tangtse Metamorphic Complex (TMC). Note the preferred alignment of biotites and
710 the lack of any alignment of the amphiboles. e) Foliation defined by a preferred orientation of
711 biotites and quartz ribbon in the deformed amphibolites. Note the high wavelength sutures
712 along the grain boundaries of quartz. f) Preferred orientation of biotites and deformed
713 lamellar twining in plagioclase in the deformed amphibolites of the TMC. d) Core-mantle
714 structures in the feldspathic domains of the granite gneisses. Note the sharp distinct
715 boundaries between the core and the mantle of recrystallized grains.

716 **Figure 4** Photomicrographs along the Tangtse strand of the KSZ: a, b) Coarse-grained
717 monomineralic quartz-rich layers (CGQL) alternating with amphibole-biotite-quartz rich
718 polymineralic layers (AMBIORL). Note the considerably finer grain size of quartz in the

AMBIORL as compared to the quartz in the CGQL. c, d) Consistent association of the finer-grained quartz with the amphibole-biotite bearing domains in the AMBIORL. Note the increase in grain-size of quartz with distance from the amphiboles and biotites. Points P and P' have been used to calculate displacement accommodated by the CGQL due to shearing along the KSZ. Points Q and Q' have been utilized to determine displacement accommodated by the ABIORL during shearing. e) Microstructure of quartz in the CGQL. Note the amoeboid grain boundaries in all directions with respect to the individual quartz grains as well as the high-wavelength sutures along the grain-boundaries f) Microstructures of quartz in both the CGQL and the AMBIORl. Note that both in the CGQL and the AMBIORL quartz grains show high wavelength sutures along amoeboid grain boundaries. Also note that pinning of quartz by amphiboles and biotites restricts GBM in quartz at high angles to the foliation in the AMBIORL.

Figure 5 Diagram (adapted from and modified after Law, 2014) showing the ranges of strain-rate at which GBM (Green dashed lines) and BLG (Yellow dashed lines) can operate in the quartz grains deformed along the KSZ at 550-600 ℃ Yellow lines. Note that for BLG operates at strain rates, at least 10^2 to 10^5 times higher than that required for GBM at 550-600 ℃. Orange dashed line represents the strain-rate values calculated along the KSZ by Boutonnet et al. (2013).

Figure 6 Schematic diagram showing the stages of evolution of the amphibolites during deformation along the KSZ. a) distribution of amphiboles, biotites and quartz in the relatively low strain domains (in the TMC) with respect to the KSZ b) Increase in strain along the mylonitic strands of the KSZ resulted in the segregation of the amphiboles and biotites into layers (AMBIORL) alternating with monomineralic quartz-rich layers (CGQL). Modal proportion of quartz in Circular area, A in the AMBIORL is lower than the modal proportion of quartz in identical circular area, A in the CGQL. c) Greater nucleation of dynamically

recrystallized grains in the AMBIORL owing to a greater accommodation of strain by the quartz at higher strain-rate per unit area, adjacent to the amphiboles and biotites (that did not accommodate significant strain) than the quartz in the CGQL, away from the amphiboles and biotites.

Figure 7 Diagram showing the variations in displacement from the micro to regional scale if strain rate is partitioned in a proportion similar to that between the CGQL and the AMBIORL in mylonitized amphibolites of the KSZ. a) Displacement accommodated by the CGQL and the AMBIORL in microscopic scale. Note that the AMBIORL accommodates displacement (d') almost 2-3 km greater than the displacement accommodated by the CGQL (d). b) Assuming similar proportion of partitioning of strain rate between hypothetical layer 1 and hypothetical layer 2 in outcrop scale, layer 2 accommodates 850-1500 m greater than that accommodated by layer 1. c) Assuming similar proportion of partitioning of strain rate between hypothetical layer 1 and hypothetical layer 2 in regional scale, layer 2 accommodates 100-200 km greater than that accommodated by layer 1.

Table 1 Table showing the values of the mean grain size (D) for the CGQL and the AMBIORL, respectively, calculated using the formulations of Christie and Ord (1980).

Appendix

Estimated displacements accommodated by the CGQL and the AMBIORL assuming that the CGQL deformed at a rate of 1.6 x 10^{-13} s^{-1} from 27-15 Ma (timing of shearing along the KSZ). Similar calculations, extrapolated to hypothetical layers 1 and 2 to have an estimate of the displacements accommodated in outcrop scale (10 m: assumed thickness of each layer) and regional scale (1.25 km: assumed thickness of each layer) under conditions of similar proportion of strain-rate partitioning, as derived in equations 13-15, between layer 1 and layer 2

Displacement accommodated by CGQL and AMBIORL (micro-scale)

If, it is assumed that quartz in the CGQL deformed at a rate of 1.6 x 10^{-13} s^{-1} (Boutonnet et al., 2013) then the quartz grains in the AMBIORL must have deformed at a rate in between

2.34(1.6 x 10^{-13}) s^{-1} to 3.43(1.6 x 10^{-13}) s^{-1}

as, $\dot{\varepsilon}_{AMBIORL}/\dot{\varepsilon}_{CGQL}$ = 2.34 to 3.43 as per equations (13) to (15)

Therefore, quartz the AMBIORL deformed at a rate of 2.34 x (1.6 x 10^{-13}) s^{-1} to 3.43 x (1.6 x 10^{-13}) s^{-1}

Considering that deformation in the CGQL and the AMBIORL operated at these rates from 27-15 Ma (Pundir et al., 2020b) i.e., for a duration of 12 Ma, strain accommodated by the two layers are:

$(Strain)_{CGQL} = \dot{\varepsilon}_{CGQL}$ x (12 x 10^6 x 365 x 24 x 60 x 60)

= 1.6 x 10^{-13} x 12 x 10^6 x 365 x 24 x 60 x 60

= 1.6 x 12 x 365 x 24 x 36 x 10^{-13} x 10^6 x 10^2

= 6054912 x 10^{-5}

= 60.5

$(Strain)_{AMBIORL} = \dot{\varepsilon}_{CGQL}$ x (12 x 10^6 x 365 x 24 x 60 x 60)

= 2.34 x (1.6 x 10^{-13} x 12 x 10^6 x 365 x 24 x 60 x 60) *to* 3.43 x (1.6 x 10^{-13} x 12 x 10^6 x 365 x 24 x 60 x 60)

= (2.34 x 60.5) to (3.43 x 60.5)

= 141.57 to 207.5

Applying equation 2,

789 Displacement (d) accommodated by CGQL = $(Strain)_{CGQL}$ x width of CGQL

790 = 60.5 x w; w: width of CGQL (Fig. 4d)

791 = 60.5 x 152.3 µm

792 = 9214.15 µm

793 = 0.92 cm (Fig. 7a)

794 Similarly, displacement (d') accommodated by AMBIORL

795 = $(Strain)_{CGQL}$ x width of AMBIORL

796 = (141.57 to 207.5) x w'; w': width of AMBIORL (Fig. 4d)

797 = (141.57 to 207.5) x 197.1 µm

798 = 27903.447 µm to 40898.35 µm = = 2.79 cm to 4.1 cm (Fig. 7a)

799 Displacement accommodated by hypothetical layers 1 and 2 (outcrop scale)

800 If similar proportion of strain-rate partitioning are extrapolated to two hypothetical layers 1
801 and 2 (each 10 m thick) (Fig. 7b) such that layer 2 deforms at a rate 2.34 to 3.43 times that of
802 layer 1 (Fig. 7b) and layer 1 deforms at 1.6 x 10^{-13} s^{-1} (Boutonnet et al., 2013) then by
803 similar calculations, over 12 Ma

804 Displacement (d) accommodated by hypothetical layer 1 = 60.5 x 10 m = 605 m (Fig. 7b)

805 and, Displacement (d) accommodated by hypothetical layer 1 = (141.57 to 207.5) x 10 m

806 = 1416 to 2075 m (Fig. 7b)

807

808

809 Displacement accommodated by hypothetical layers 1 and 2 (regional scale):

810 If similar proportion of strain-rate partitioning are extrapolated to two hypothetical layers 1
811 and 2 (each 1.25 km thick) (Fig. 7c) such that layer 2 deforms at a rate 2.34 to 3.43 times that
812 of layer 1 (Fig. 7c) and layer 1 deforms at 1.6 x 10^{-13} s^{-1} (Boutonnet et al., 2013) then by
813 similar calculations, over 12 Ma

814 Displacement (d) accommodated by hypothetical layer 1 = 60.5 x 1.25 km = 75.625 km (Fig.
815 7c)

816 and, Displacement (d) accommodated by hypothetical layer 1 = (141.57 to 207.5) x 1.25 km

817 = 177 to 259.37 km (Fig. 7c)

818

819 Thus, in micro scale AMBIORL accommodates a displacement, 1.87-3.18 cm greater than
820 the CGQL. When strain-rate is partitioned in a proportion equal to $\dot{\varepsilon}_{AMBIORL}/\dot{\varepsilon}_{CGQL}$, between
821 hypothetical layers 1 and 2, layer 2 accommodates displacement 811-1470 m and 101-183
822 km greater than layer 1 in outcrop scale and regional scale, respectively.

823

824

LAYER IN MYLONITIZED AMPHIBOLITE (TM 2)	**MEAN GRAIN SIZE (D; calculated after Christie and Ord, 1980)**
Coarse grained quartz rich layer (CGQL)	127.5796 µm
Amphibole-biotite rich layer (AMBIORL)	57.83167 µm

Figure 1.

a

N

ATF

Karakoram

KF

Tibetan P.

STD

INDIA

Karakoram Batholith

Ladakh Batholith

Indus Suture

ATF- Altyn Tagh Fault

KF- Karakoram Fault

STD- South Tibet Detachment

0 100 200

Km

.Kathmandu

b

78°15´E

SHYOK R.

Kunzang lungpa

N

W AF

E. AF

Phobrang

Lukung

PANGONG TSO

78°30´E

SHYOK R.

Shyok

DS 8

DS 7

DS 6

Muglib

Tangtse

TM 2

TM 1

Durbuk

KF

KF

77°45´E

Rongdo

Tsati

Agham

Tsoltak

Chang La

78°15´E

INDEX

Indus Tsangpo Suture Zone

Ladakh Batholith

Shyok Suture Zone

Undeformed South Tangtse Granite

Karakoram Shear Zone

Muglib Leucogranite

Tangtse Metamorphic Complex

Agham Metamorphics

Shyok Metamorphic Complex

Pangong Metamorphic Complex: Slate, Schist, Marble, Amphibolite

Karakoram Batholith

Murgo Volcanics

Karakoram Metamorphics Undifferentiated

0 km 10

34°15N´

34°0N´

33°45N´

Figure 2.

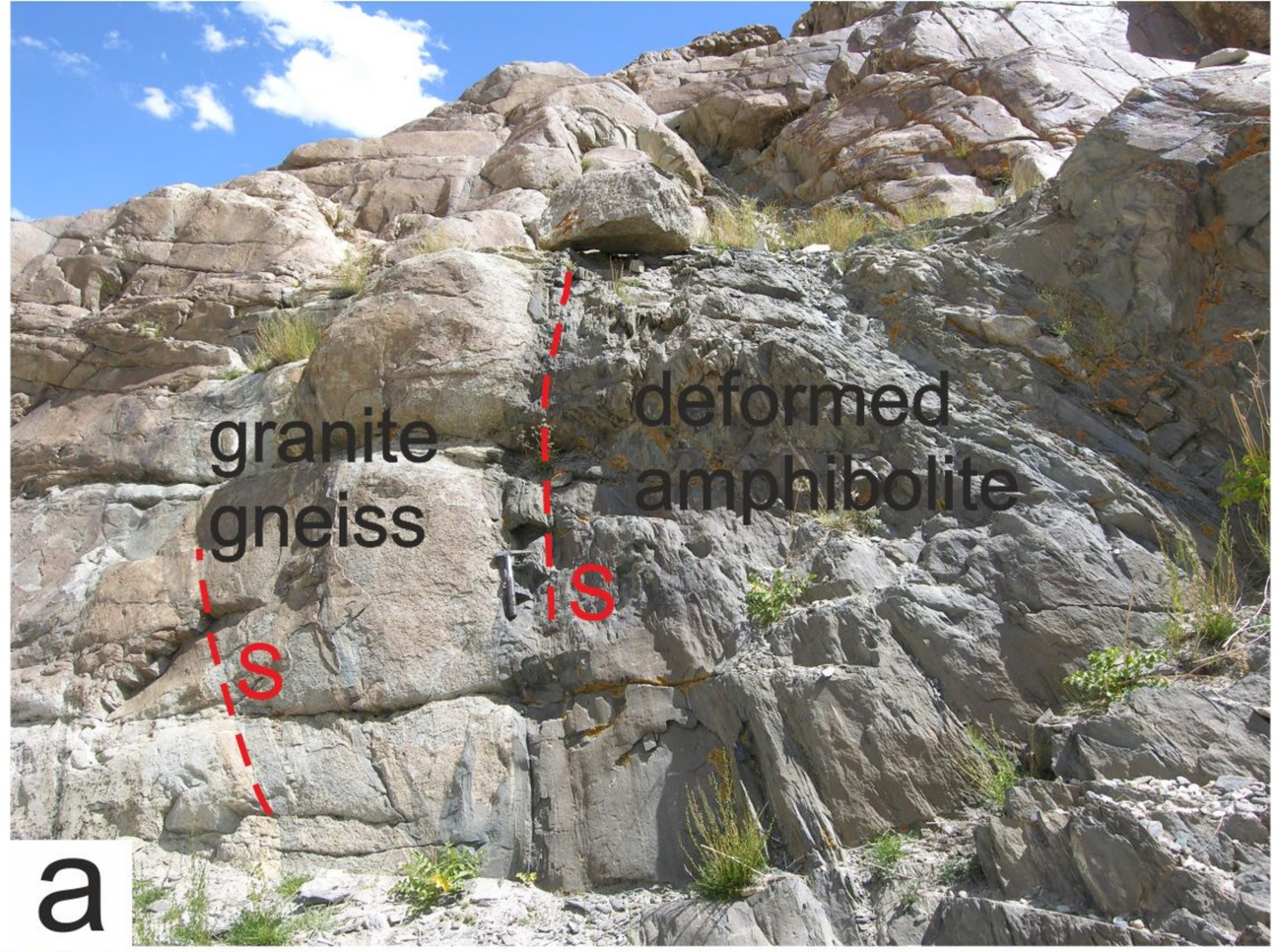

a

b

c

d

Figure 3.

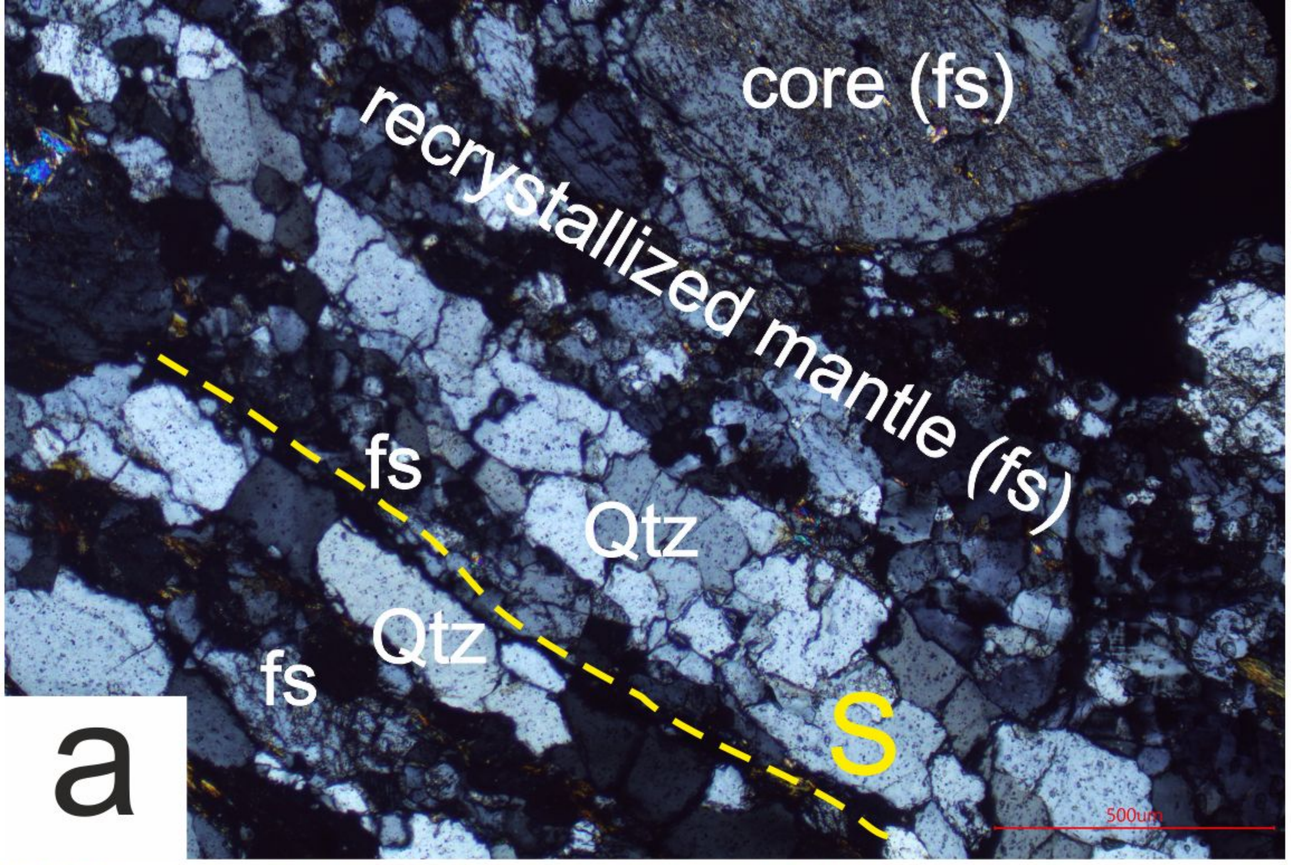
core (fs)
recrystallized mantle (fs)
fs
Qtz
Qtz
fs
S
500um

a

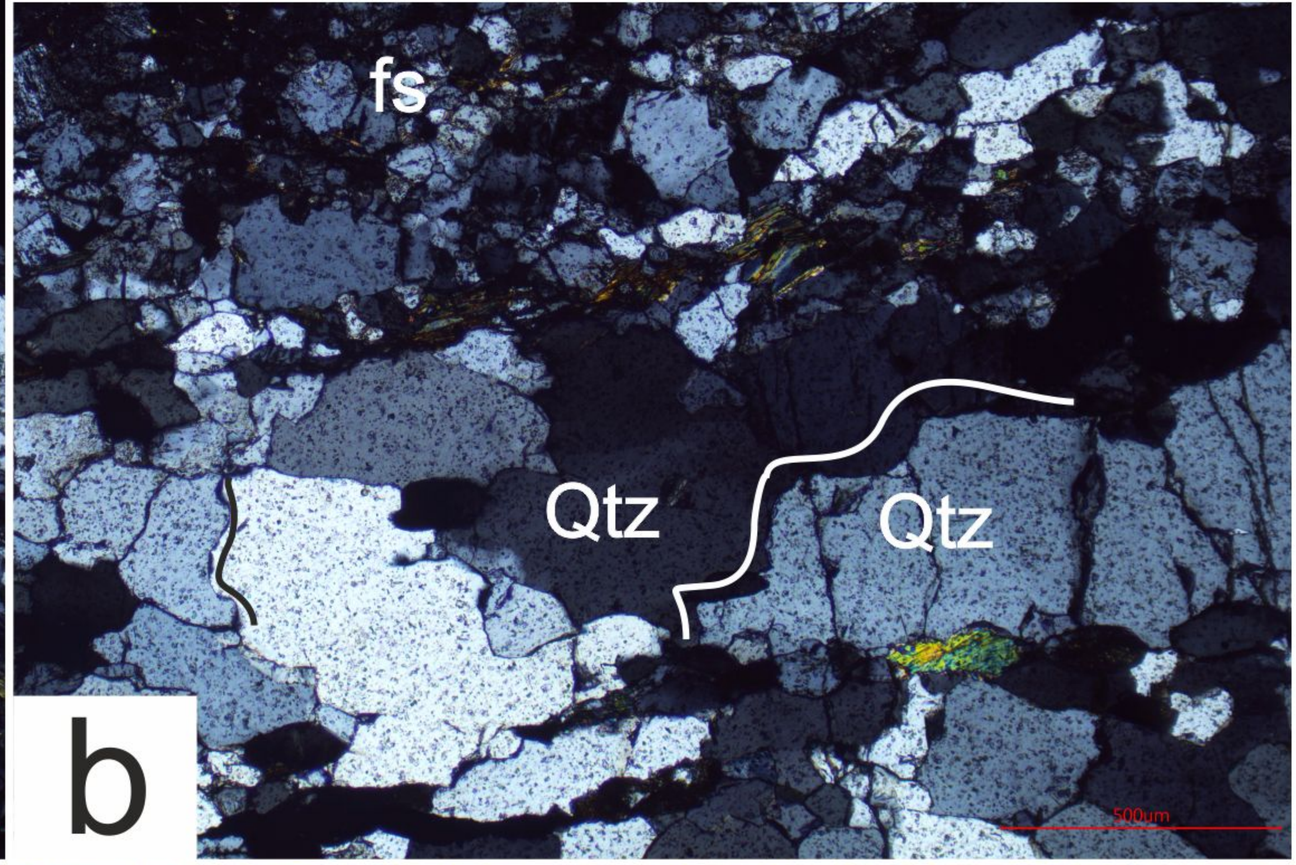
fs
Qtz
Qtz
500um

b

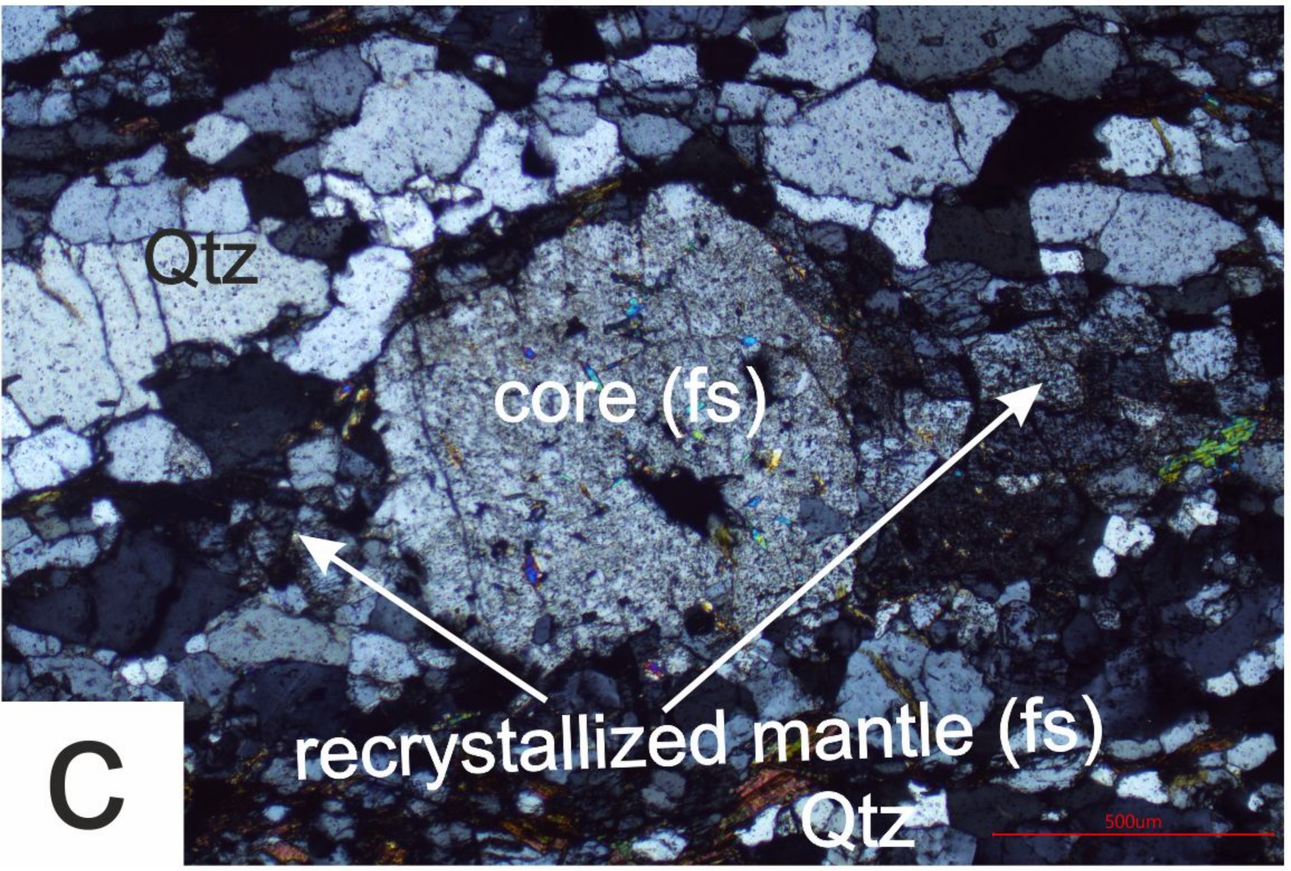
Qtz
core (fs)
recrystallized mantle (fs)
Qtz
500um

c

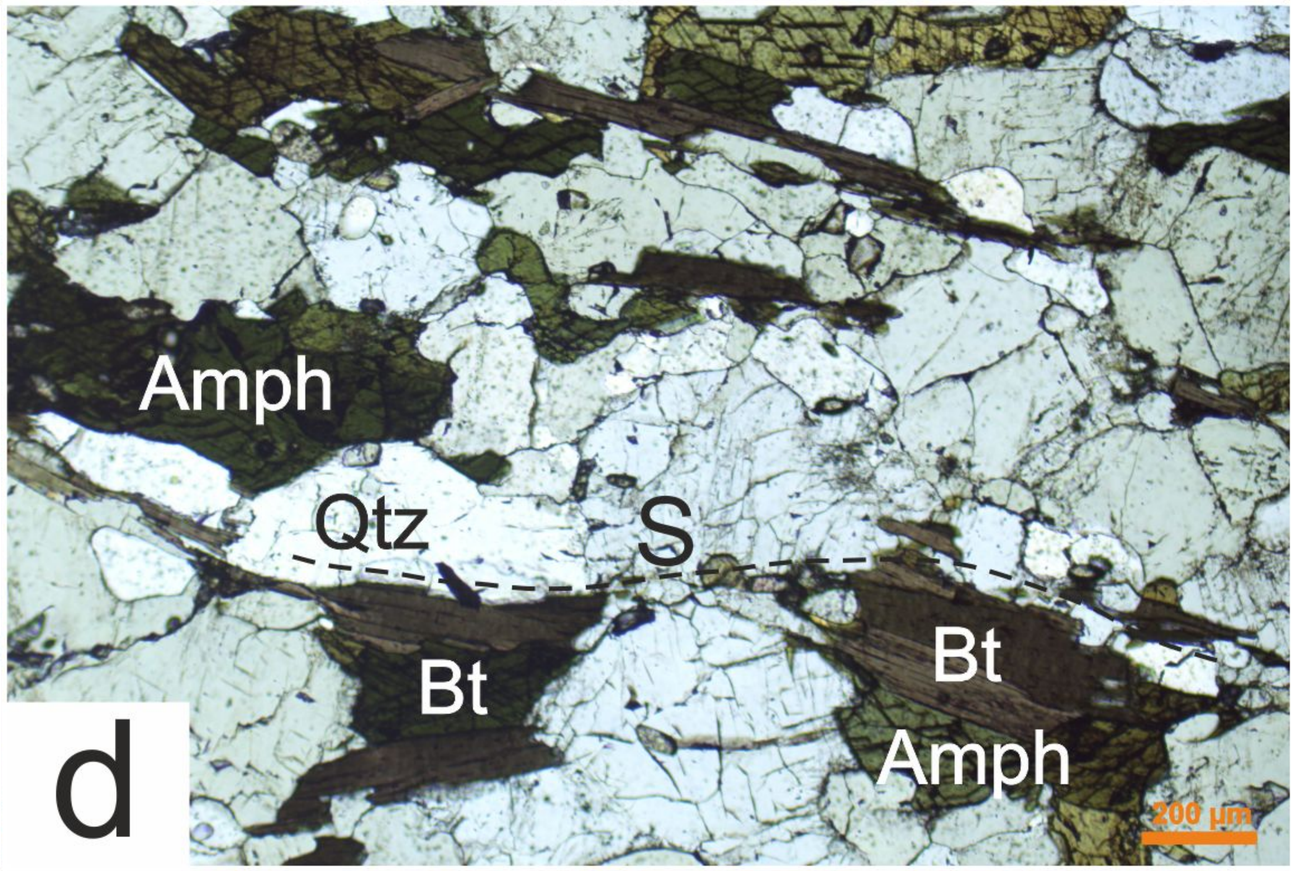
Amph
Qtz
S
Bt
Bt
Amph
200 µm

d

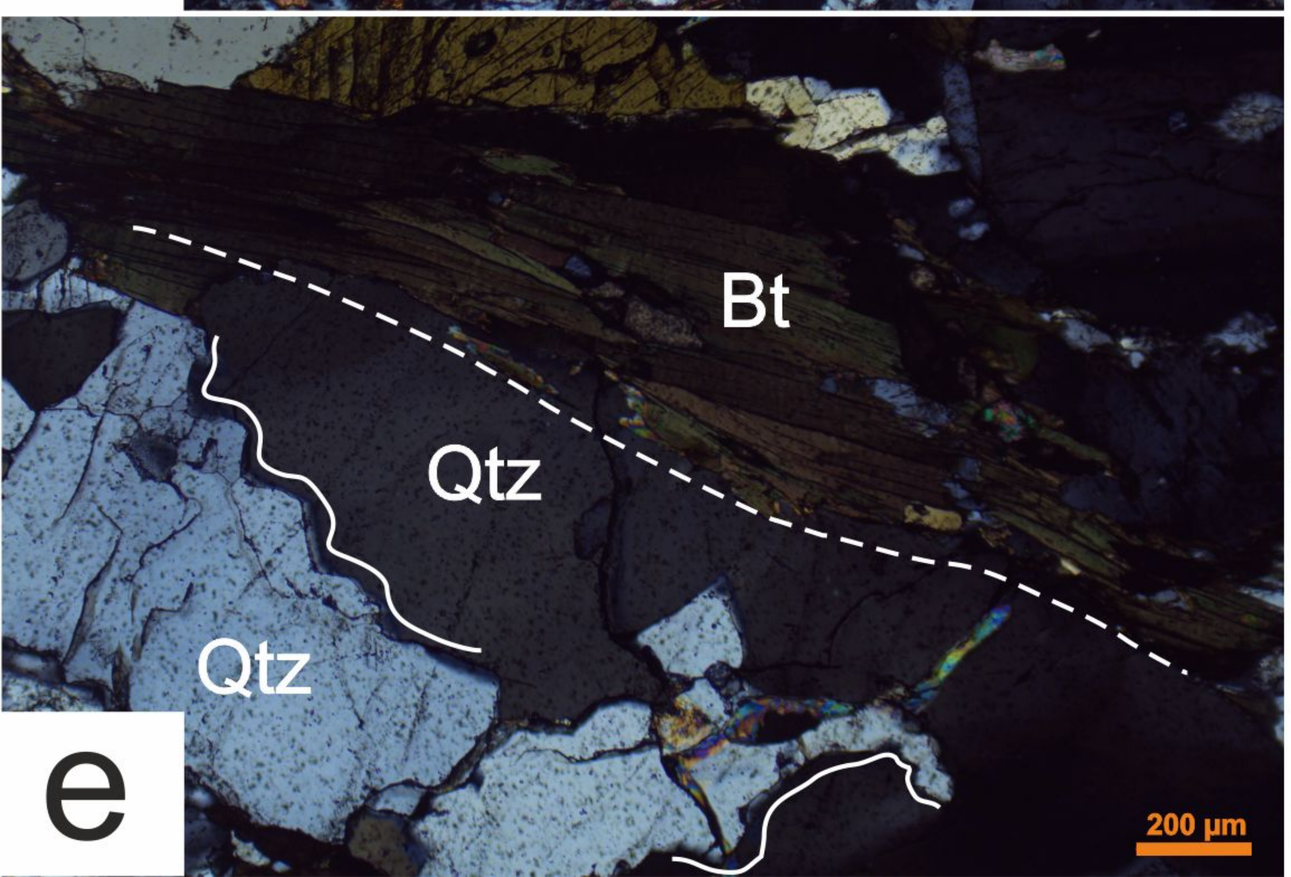
Bt
Qtz
Qtz
200 µm

e

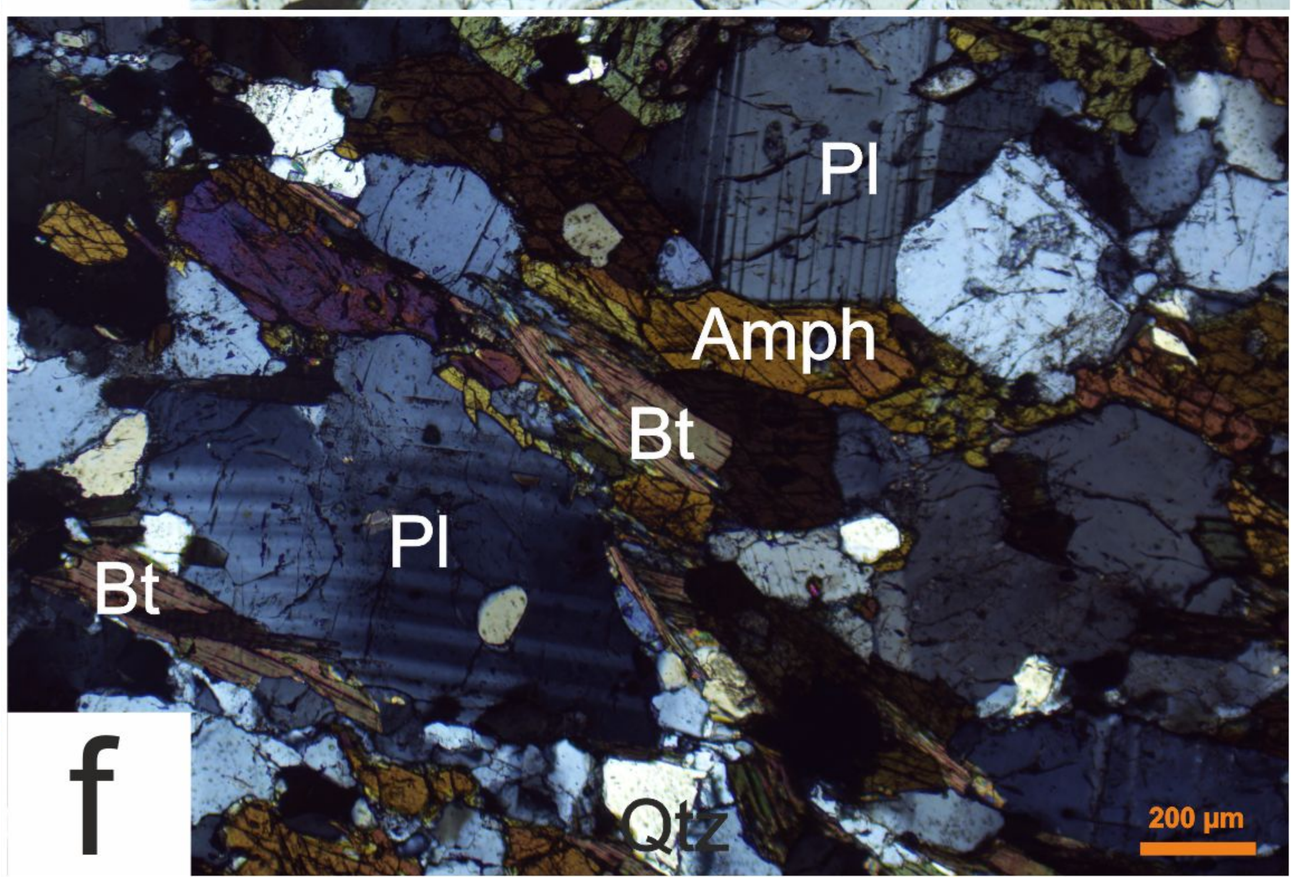
Pl
Amph
Bt
Pl
Bt
Qtz
200 µm

f

Figure 4.

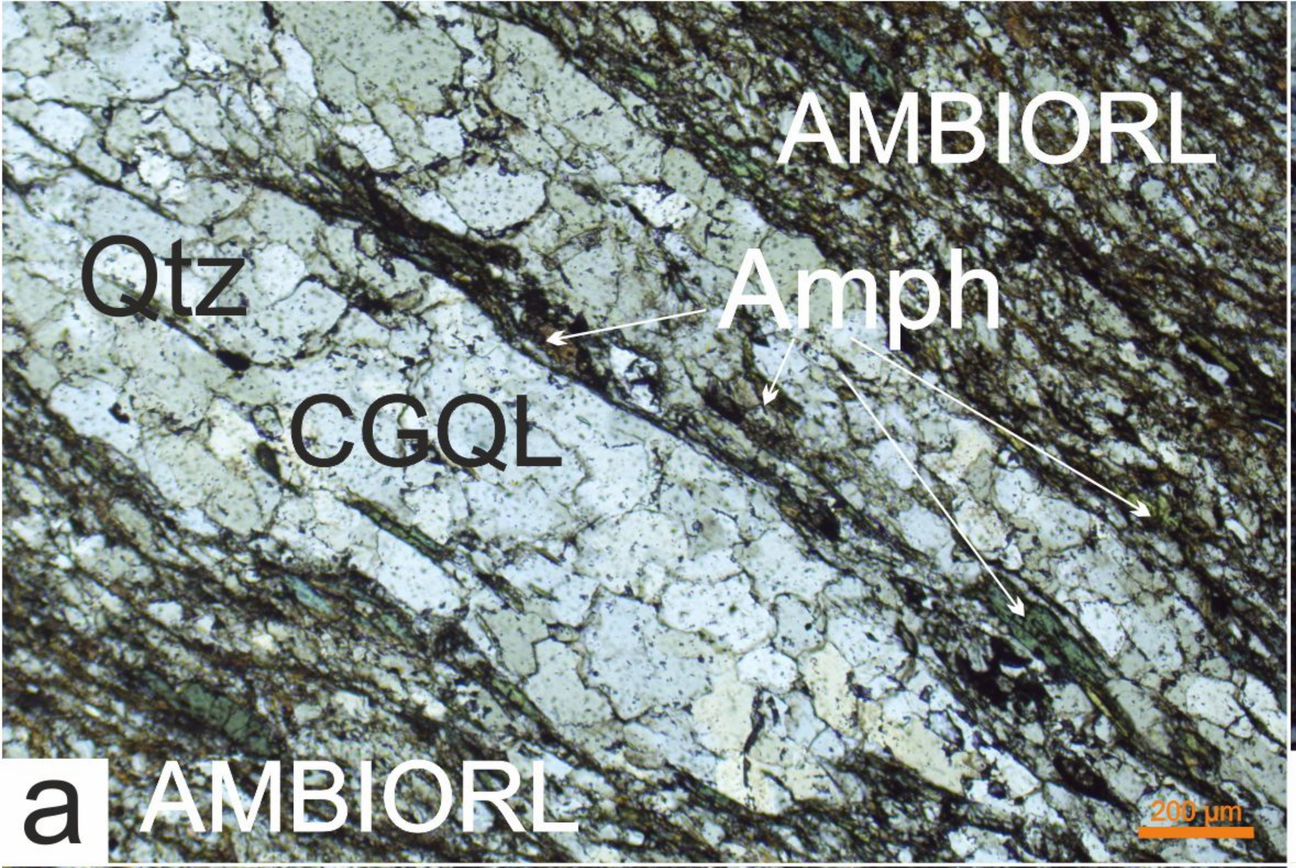
AMBIORL
Qtz
Amph
CGQL
a
AMBIORL
200 µm

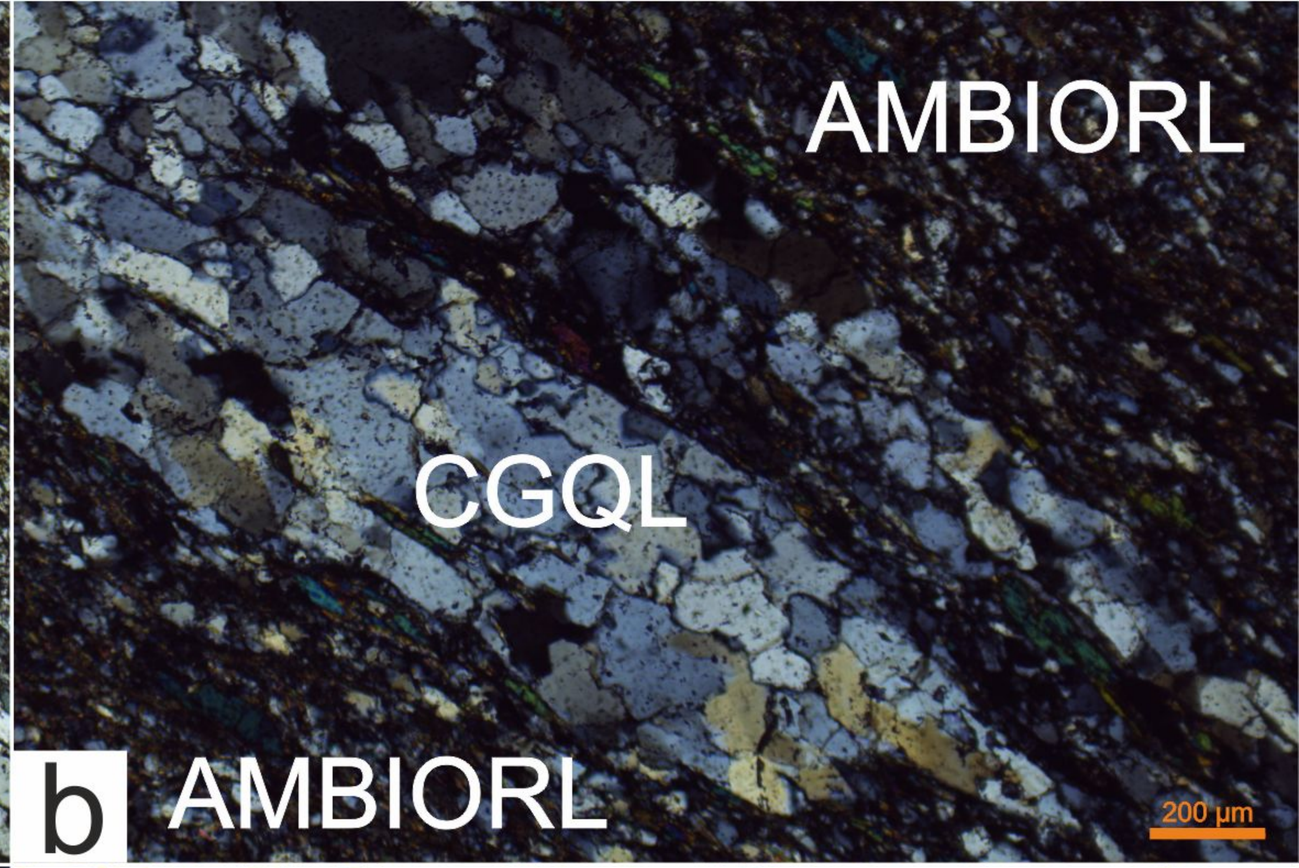
AMBIORL
CGQL
b
AMBIORL
200 µm

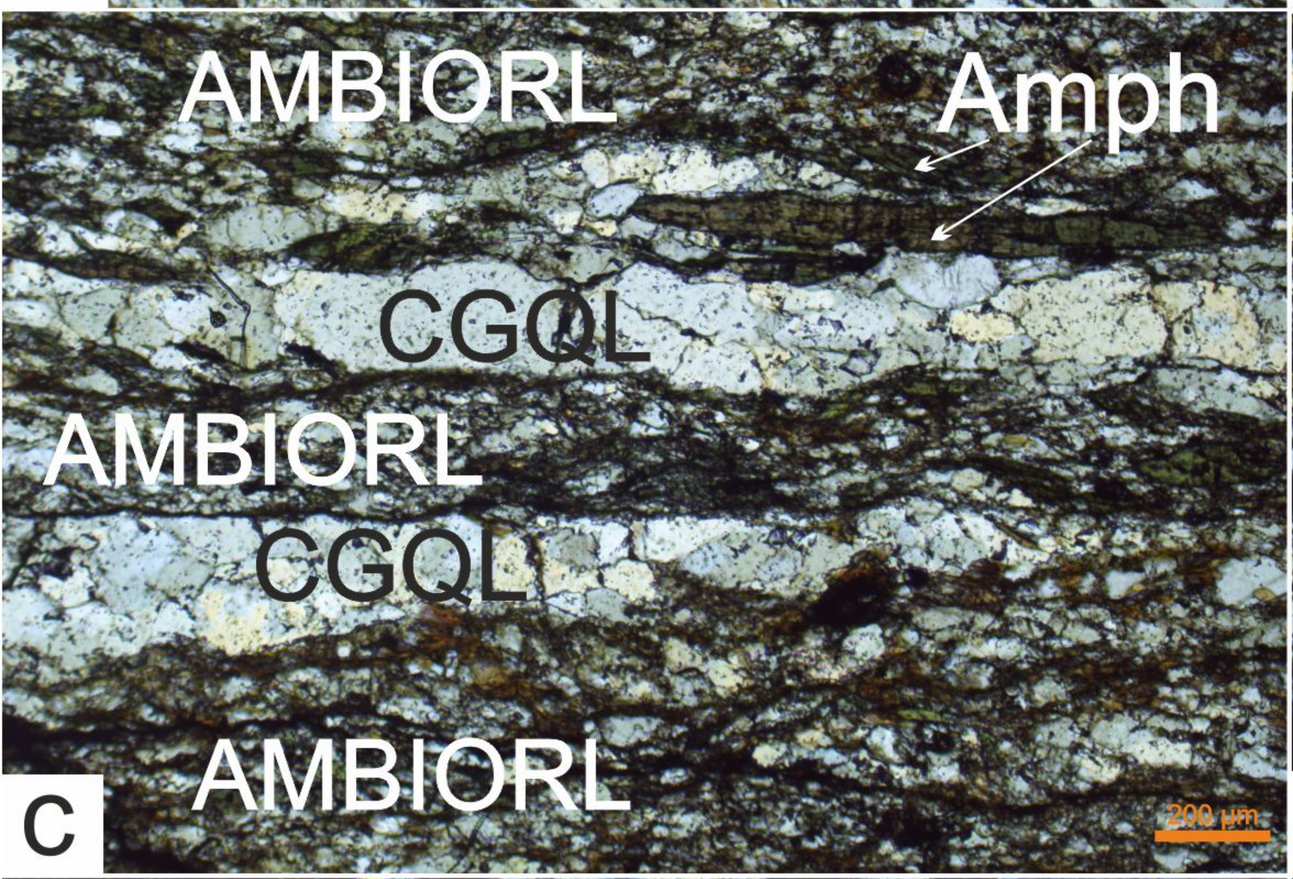
AMBIORL
Amph
CGQL
AMBIORL
CGQL
AMBIORL
c
200 µm

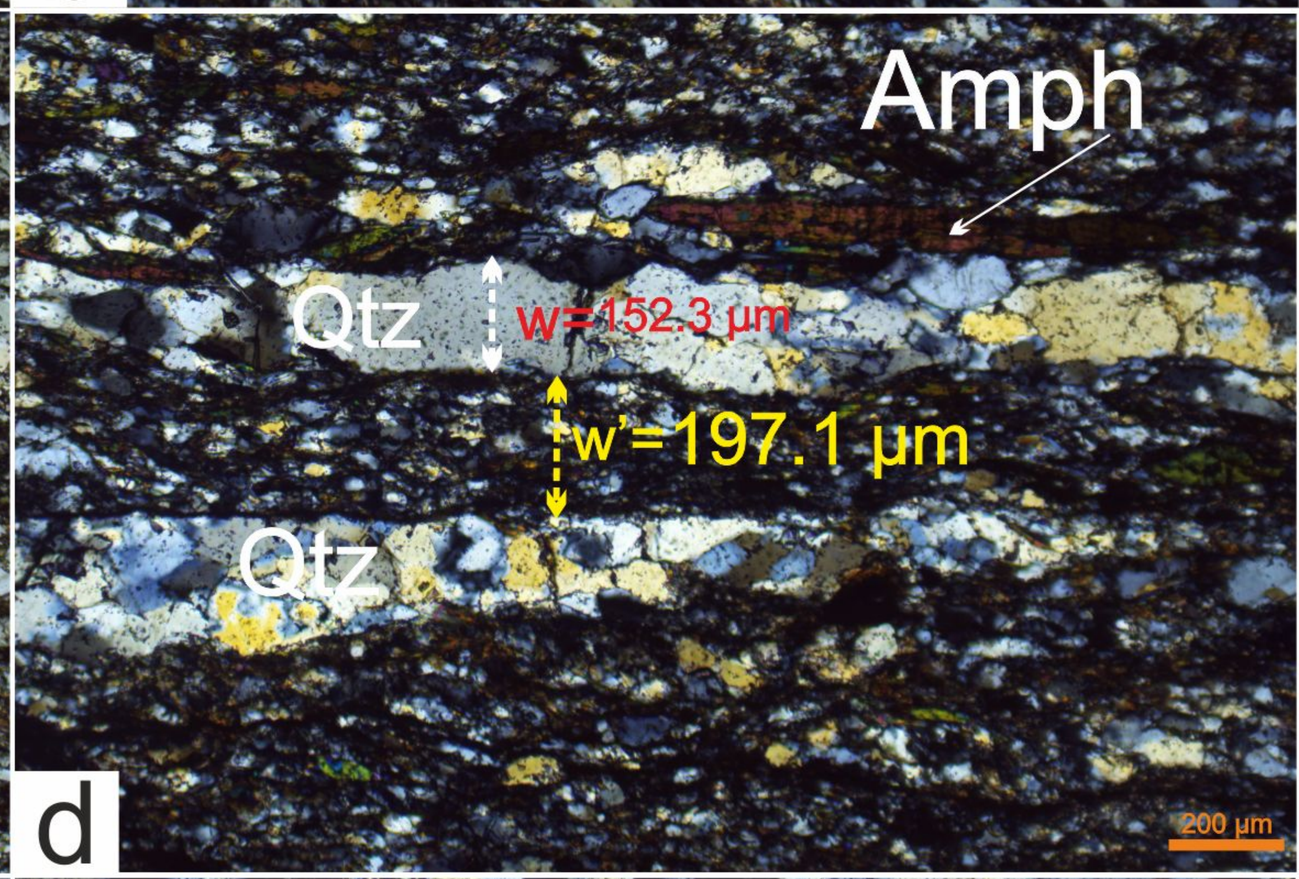
Amph
Qtz
w=152.3 µm
w'=197.1 µm
Qtz
d
200 µm


Qtz
e
200 µm

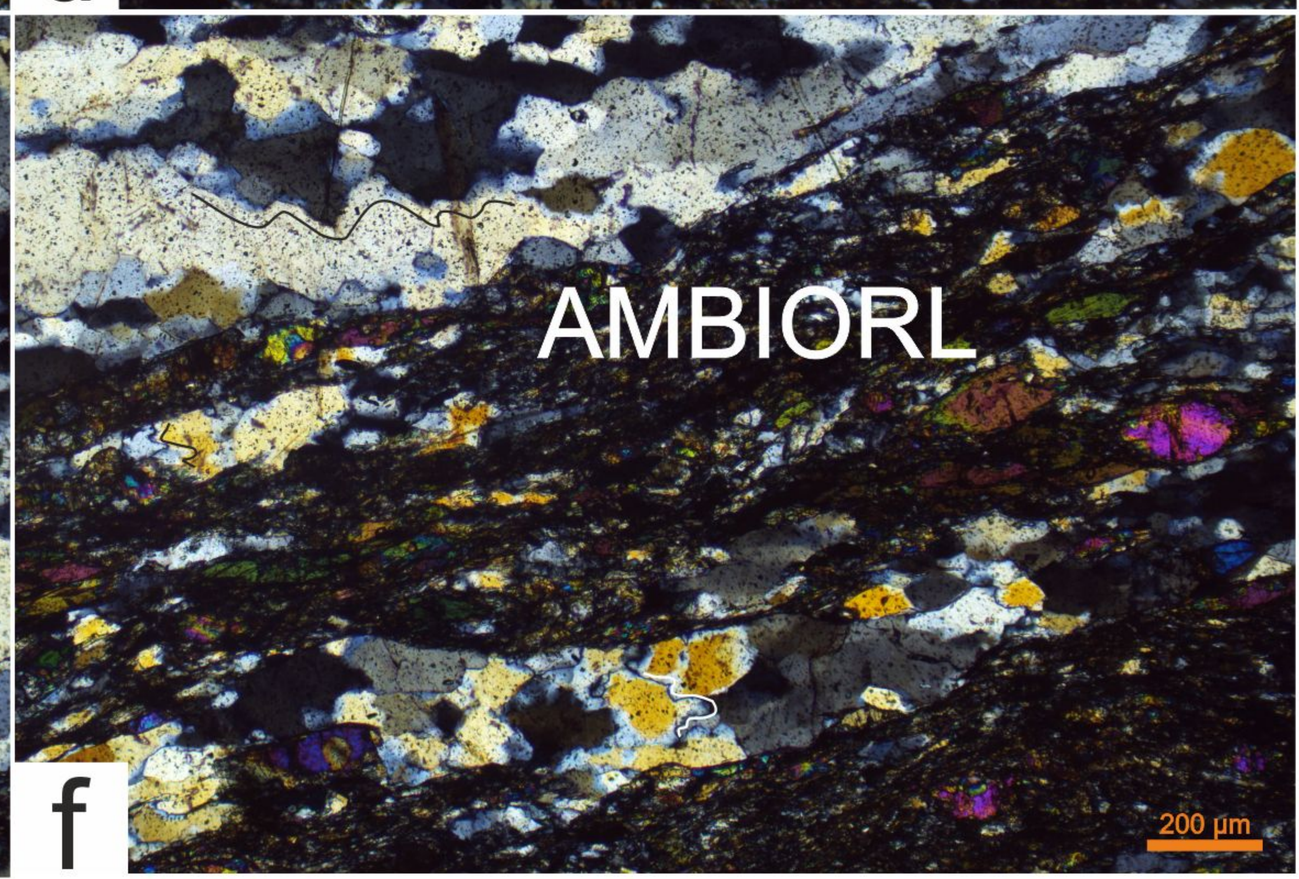
AMBIORL
f
200 µm

Figure 5.

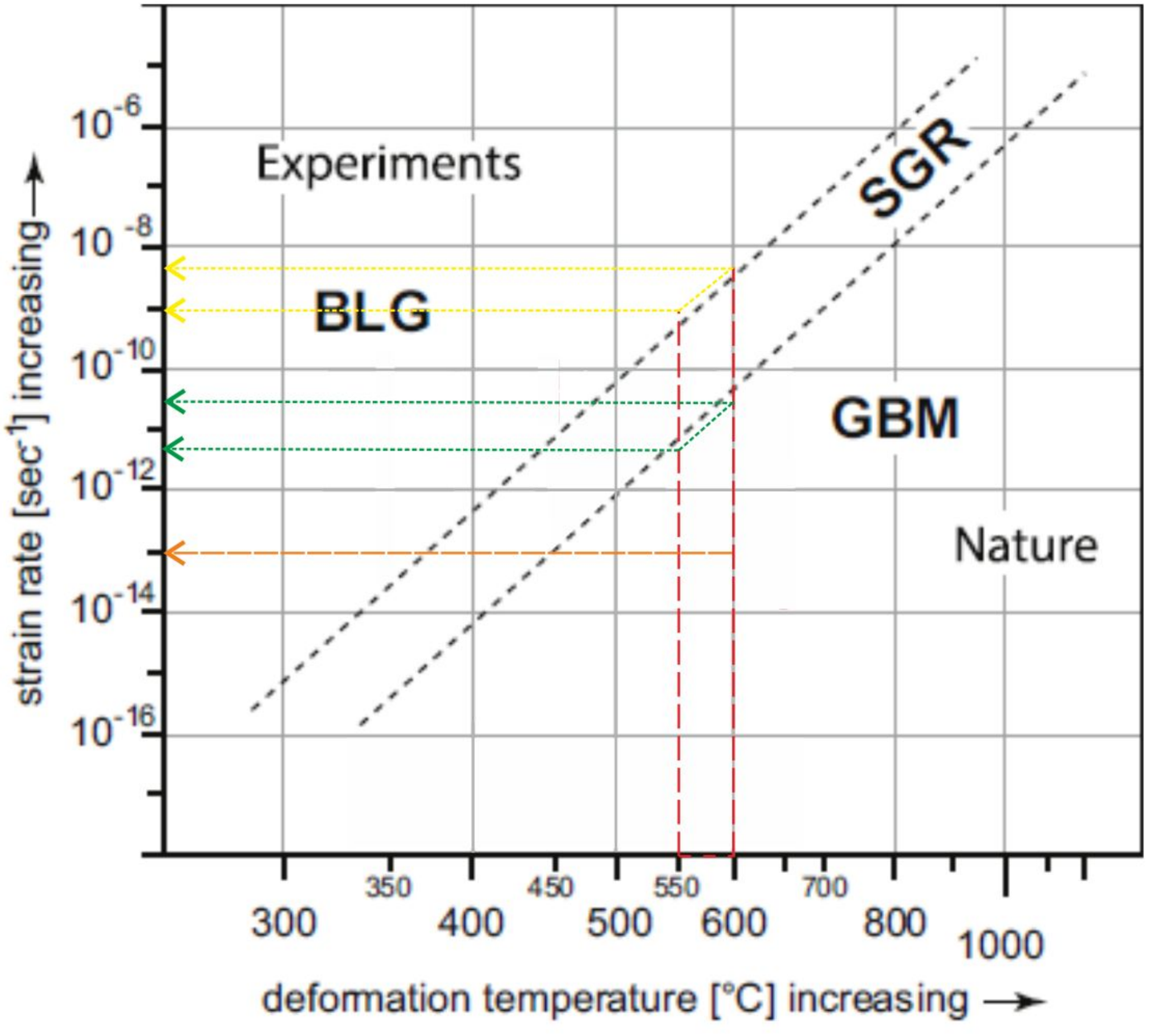

estimated strain-rates for BLG in quartz at 550-600 degree C

estimated strain-rates for GBM in quartz at 550-600 degree C

calculated strain-rate of quartz along the mylonitic strands of the KSZ (Boutonnet et al., 2013)

Figure 6.

Low strain

a

higher strain per unit area of quartz in the AMBIORL

b

lower strain per unit area of quartz in monomineralic quartz-rich layers

lower strain rate per unit area of quartz in the CGQL

higher strain rate per unit area of quartz in the AMBIORL

C

CGQL

AMBIORL

High strain

quartz

amphibole

biotite

Figure 7.

MICRO SCALE
(mylonitized amphibolite)

$\dot{\epsilon}_{AMBIORL} = (2.34 \text{ to } 3.43) \times \dot{\epsilon}_{CGQL}$

CGQL — w = 152.3 μm — d = 0.92 cm

AMBIORL — w' = 197.1 μm — d' = 2.79-4.1 cm

a

OUTCROP SCALE
(hypothetical)

$\dot{\epsilon}_{layer\ 2} = (2.34 \text{ to } 3.43) \times \dot{\epsilon}_{layer\ 1}$

hypothetical layer 1 — w = 10 m — d = 605 m

hypothetical layer 2 — w' = 10 m — d' = 1416-2075 m

b

REGIONAL SCALE
(hypothetical)

$\dot{\epsilon}_{layer\ 2} = (2.34 \text{ to } 3.43) \times \dot{\epsilon}_{layer\ 1}$

2.5 km

hypothetical layer 1 — w = 1.25 km — d = 75.625 km

hypothetical layer 2 — w' = 1.25 km — d' = 177 to 259.37 km

c